

# Stacking-Directed Polarization and Excitonic Engineering in MoS<sub>2</sub>/MoSe<sub>2</sub> van der Waals Heterostructures

Mohammed El Amine Miloudi , Oliver Kühn 

Institute of Physics, University of Rostock, Albert-Einstein-Str. 23–24, D-18059 Rostock, Germany

E-mail: oliver.kuehn@uni-rostock.de

8 July 2026

**Abstract.** The stacking-dependent polarization and excitonic response of MoS<sub>2</sub>/MoSe<sub>2</sub> heterostructures were investigated using GW+BSE many-body perturbation theory. While homobilayer MoS<sub>2</sub> exhibited a switchable interlayer dipole driven by registry-induced symmetry breaking, the MoS<sub>2</sub>/MoSe<sub>2</sub> hetero-interface remained pinned by the intrinsic chemical potential mismatch between sulfur and selenium. In 2L-MoS<sub>2</sub>/MoSe<sub>2</sub> trilayers, the stacking sequence enabled a deterministic control of photogenerated electrons between the central and bottom MoS<sub>2</sub> layers, governed by internal electric fields and quasiparticle band-edge shifts of 60–70 meV. Our calculations predicted a 36 meV interlayer excitonic shift, in remarkable agreement with recent experiments. These results elucidate the microscopic link between atomic registry and many-body interactions, establishing transition metal dichalcogenide trilayers as a potential platform for sliding ferroelectricity and programmable optoelectronic functionalities.

## 1. Introduction

Two-dimensional (2D) van der Waals (vdW) heterostructures, formed by stacking atomically thin crystals via weak interlayer interactions, have emerged as highly versatile platforms for exploring quantum phenomena and engineering optoelectronic functionalities beyond what bulk materials can offer [1–7]. The vdW nature of these interactions facilitates precise control over stacking sequence, rotational alignment, and interlayer spacing, giving rise to Moiré superlattices and enabling atomic-scale tuning of electronic band structures, excitonic resonances, and interfacial polarization. These properties make vdW heterostructures ideal for manipulating light–matter interactions at the atomic scale.

Among 2D materials, transition metal dichalcogenides (TMDs) such as MoS<sub>2</sub>, MoSe<sub>2</sub>, WS<sub>2</sub>, and WSe<sub>2</sub> have attracted particular attention due to their direct band gaps in the visible–near-infrared range, strong spin–orbit coupling, and tightly bound excitons with binding energies of 0.5–0.9 eV [8–12]. These high binding energies, nearly an order of magnitude larger than in conventional bulk semiconductors, arise from

reduced dielectric screening and enhanced Coulomb interactions in two dimensions. Consequently, monolayer TMDs exhibit exceptionally strong light absorption, up to 5–10% of incident light per layer, and robust valley-selective optical transitions, making them ideal candidates for excitonic and valleytronic applications [10, 11, 13].

When stacked into heterostructures, TMD monolayers often display type-II band alignment, which spatially separates electrons and holes and stabilizes interlayer excitons with large out-of-plane dipole moments and extended lifetimes [7, 11]. For instance, in  $\text{MoS}_2$ -based heterostructures, conduction- and valence-band offsets of 0.3–0.6 eV drive ultrafast interlayer charge transfer on sub-100 fs timescales [14, 15]. The spatial separation of carriers suppresses radiative recombination and renders interlayer excitons highly sensitive to interfacial asymmetry and external fields, providing versatile opportunities for optoelectronic and quantum-functional devices.

The electronic and excitonic properties of vdW heterostructures are strongly dependent on interlayer arrangement, atomic registry, and stacking symmetry. Variations in stacking alter interlayer orbital hybridization, local electrostatics, and charge distribution, which in turn modify band edges, exciton binding energies, and optical selection rules. In twisted heterobilayers, small relative rotations produce long-period Moiré superlattices that confine electrons, holes, and interlayer excitons, flatten excitonic minibands, and enable discrete exciton arrays with correlated phases and single-photon emission [16–20]. For twist angles below approximately  $2^\circ$ , Moiré periods can exceed 10–15 nm, generating deep periodic potentials that strongly influence exciton localization and recombination dynamics.

Interlayer excitons in TMD heterobilayers exhibit lifetimes that are orders of magnitude longer than those of intralayer excitons, reflecting their spatially indirect character. For example, vertically stacked  $\text{MoSe}_2\text{--WSe}_2$  heterostructures show interlayer exciton lifetimes of approximately 1.8 ns at low temperature, compared to tens of picoseconds for intralayer excitons [21]. Moiré engineering at small twist angles can further extend lifetimes into the tens-of-nanoseconds range by suppressing nonradiative decay pathways [22]. These long-lived excitons, combined with strong binding energies, underpin robust light–matter interactions and highlight the potential of vdW heterostructures for excitonic devices.

While Moiré superlattices provide a static landscape for particle localization, lateral interlayer sliding offers a continuous and dynamical pathway to sample the stacking configuration space without changing the Moiré period [23, 24]. By systematically shifting the stacking configuration, sliding can reversibly modulate interfacial polarization, band topology, charge transfer, and exciton energies. This registry-dependent control complements Moiré engineering, enabling the design of heterostructures with electrically controllable dipoles and tailored excitonic landscapes [25, 26].

The interplay between interlayer polarization and excitonic dynamics opens additional avenues for quantum-functional design. In inversion-asymmetric or 3R-stacked TMD heterostructures, spontaneous out-of-plane polarizations on the order of

0.1–0.3 C m<sup>-2</sup> produce internal fields up to 0.1–0.5 V nm<sup>-1</sup>, sufficient to shift band edges, redistribute charge, and tune interlayer exciton energies [27, 28]. Controlled stacking and polarization engineering thus enable electrically programmable excitonic landscapes, ferroelectric switching, and multifunctional optoelectronic behavior [29].

Despite these advances, a systematic understanding of how atomic registry governs many-body excitonic behavior in MoS<sub>2</sub>-based heterostructures remains elusive. Existing theoretical frameworks often rely on mean-field approximations that fail to account for the non-local screening and enhanced Coulomb interactions inherent to these 2D interfaces. Consequently, the fundamental relationship between local stacking order and the resulting interfacial dipoles particularly at the many-body GW–BSE level requires in-depth elucidation. This motivates a rigorous computational study of the electronic and excitonic landscapes in these systems.

Here, we employ a high-fidelity theoretical framework to investigate stacking-dependent polarization and excitonic properties in MoS<sub>2</sub>-based vdW heterostructures, building upon recent experimental demonstrations of ferroelectric control in 3R-stacked systems [29]. Utilizing density functional theory (DFT) with hybrid functionals and many-body perturbation theory within the EVGW<sub>0</sub> (eigenvalue-self-consistent GW<sub>0</sub>)–BSE framework, we move beyond standard approximations to precisely quantify how atomic registry and interlayer asymmetry govern interfacial dipoles and quasiparticle band alignments. We demonstrate that AB and BA registries generate interfacial dipoles of opposite polarity, resulting in switchable band-edge shifts while maintaining the robust type-II alignment necessary for charge separation. Furthermore, we show that in trilayer configurations, stacking-induced asymmetry allows for the fine-tuning of polarization states and excitonic transitions, offering a predictive road map for the design of non-volatile excitonic transistors and atomically controlled ferroelectric optoelectronic logic.

## 2. Computational Framework

The structural and electronic properties of MoS<sub>2</sub>/MoSe<sub>2</sub> heterostructures were investigated within the framework of DFT, as implemented in the Vienna *Ab initio* Simulation Package (VASP) [30–33]. Electron–ion interactions were described using the projector-augmented wave (PAW) formalism, with valence configurations of Mo (4s<sup>2</sup>4p<sup>6</sup>4d<sup>5</sup>5s<sup>1</sup>), S (3s<sup>2</sup>3p<sup>4</sup>), and Se (4s<sup>2</sup>4p<sup>4</sup>). Exchange–correlation effects were treated within the generalized gradient approximation using the Perdew–Burke–Ernzerhof functional [34], supplemented by Grimme’s D3 scheme to account for long-range dispersion interactions.

All calculations were performed using a plane-wave kinetic-energy cutoff of 450 eV and  $\Gamma$ -centered Monkhorst–Pack  $k$ -point meshes of  $12 \times 12 \times 1$ . A vacuum region exceeding 20 Å was introduced along the out-of-plane direction to suppress spurious interactions between periodic replicas. Atomic coordinates were fully optimized until residual forces were below 0.01 eV Å<sup>-1</sup> and total-energy variations were smaller than

$10^{-8}$  eV.

Commensurate heterostructure models were constructed by first optimizing isolated  $\text{MoS}_2$  and  $\text{MoSe}_2$  monolayers. Monolayers of  $\text{MoS}_2$  and  $\text{MoSe}_2$  were found to have lattice constants of 3.166 Å and 3.295 Å, respectively. For bilayers and heterobilayers, AA, AB, and BA stacking configurations were considered, while multiple trilayer stackings (AAA, ABA, ABB, BAA, BAB, AAB, and BBA) were systematically analyzed. Lattice matching in heterobilayers was achieved by adopting a common in-plane lattice parameter, which corresponds to biaxial strains of +2.1% in  $\text{MoS}_2$  and -1.9% in  $\text{MoSe}_2$ .

Electronic band structures and band gaps were evaluated at multiple theoretical levels. DFT calculations were performed using PBE, including spin-orbit coupling (SOC) where indicated, as well as the screened hybrid HSE06 functional without SOC. Many-body effects beyond DFT were incorporated through  $\text{EVGW}_0\text{@PBE}$  [35, 36], in which quasiparticle energies in the Green’s function were iteratively updated while the orbitals and screened Coulomb interaction were kept fixed at the PBE level. Excitonic effects in the optical response were explicitly treated by solving the Bethe–Salpeter equation (BSE) [37, 38].

All  $\text{EVGW}_0$  and BSE calculations employed PAW datasets optimized for many-body perturbation theory, including semicore states, together with carefully converged  $k$ -point meshes and numbers of unoccupied bands. Bilayer  $\text{MoS}_2$  and  $\text{MoS}_2/\text{MoSe}_2$  heterobilayer were computed using a  $\Gamma$ -centered  $12 \times 12 \times 1$   $k$ -point grid with 32 unoccupied bands, while the 2L- $\text{MoS}_2/\text{MoSe}_2$  systems used a  $\Gamma$ -centered  $9 \times 9 \times 1$  grid with 64 unoccupied bands. All numerical parameters were systematically tested to ensure the reliability of quasiparticle energies and excitonic spectra.

### 3. Results and Discussion

#### 3.1. Bilayer $\text{MoS}_2$ and $\text{MoS}_2/\text{MoSe}_2$ Heterobilayers

##### 3.1.1. Stacking-Dependent Polarization and Interlayer Charge Redistribution

The impact of stacking registry on interlayer coupling in both homobilayer  $\text{MoS}_2$  and  $\text{MoS}_2/\text{MoSe}_2$  heterobilayers was systematically evaluated for AA, AB, and BA configurations. The calculated in-plane lattice constants ( $a$ ) and out-of-plane lattice parameters ( $c$ ) for monolayer and bilayer stackings are summarized in Table S1, providing a quantitative basis for subsequent analysis of interlayer interactions.

Following full structural relaxation, the AA registry preserves high structural symmetry, whereas the staggered AB and BA configurations break global inversion symmetry, thereby inducing a finite out-of-plane electric polarization,  $P_z$ . The optimized geometries for these polar registries, including both top and side views, are illustrated for the homobilayer in Fig. 1a,b and for the heterobilayer in Fig. 1c,d, respectively. Corresponding views of the non-polar AA stacking are provided in Fig. S1a,b of the Supplemental Material (Suppl. Mat.).

The evolution of the lattice parameters from monolayer to bilayer provides insight

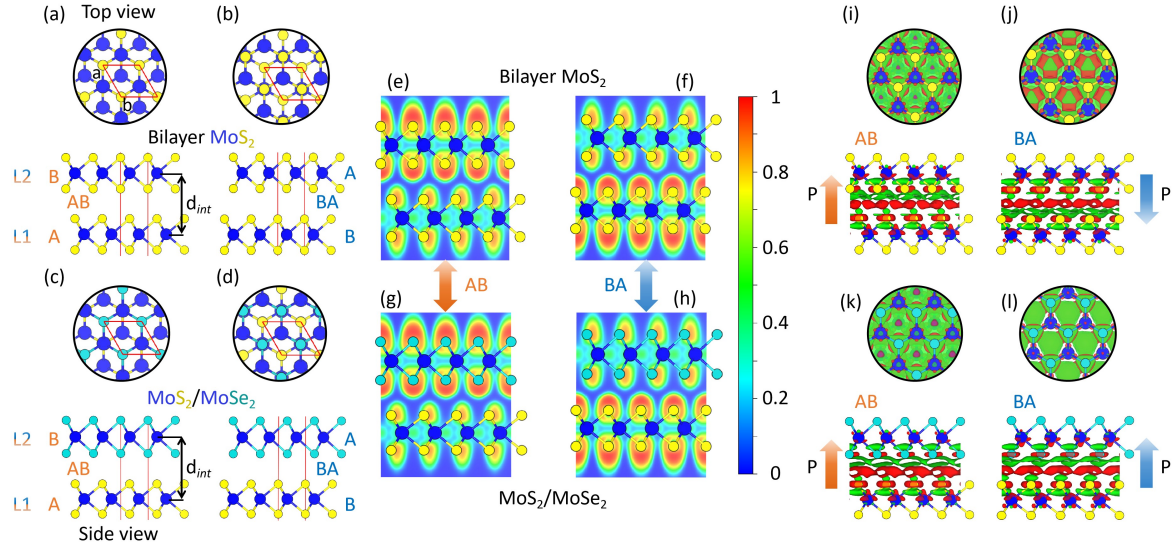


Figure 1: Top and side views of the atomic configurations for (a) AB-stacked and (b) BA-stacked  $\text{MoS}_2$  homobilayers, and (c) AB-stacked and (d) BA-stacked  $\text{MoS}_2/\text{MoSe}_2$  heterobilayers. Panels (e)–(h) display the corresponding electron localization function (ELF) contour plots with an interval of 0.1, illustrating the covalent nature of intralayer bonding and the vdW gap. Panels (i)–(l) show the charge density difference ( $\Delta\rho$ ) isosurfaces for each configuration. Red and green regions represent charge depletion and accumulation, respectively, visualized at an isovalue of  $0.001 e/\text{\AA}^3$ . The variations in stacking order and chemical composition significantly modulate the interlayer coupling and the resulting interfacial charge redistribution.

into the interplay between intralayer strain, interlayer steric repulsion, and vdW interactions. As listed in Table S1, monolayer  $\text{MoS}_2$  and  $\text{MoSe}_2$  exhibit equilibrium in-plane lattice constants of  $3.166 \text{ \AA}$  and  $3.295 \text{ \AA}$ , respectively. Upon forming a heterobilayer, the in-plane lattice constant  $a$  converges to approximately  $3.228 \text{ \AA}$ , effectively representing an arithmetic mean of the constituent monolayers. This indicates a commensurate strain regime in which the energy cost of stretching  $\text{MoS}_2$  is balanced by compressing  $\text{MoSe}_2$ , enabling commensurable stacking with minimal total elastic energy. For the homobilayer  $\text{MoS}_2$ , AB and BA stackings show only minor deviations from the monolayer  $a$  due to symmetric strain distribution between identical layers.

The out-of-plane lattice constant  $c$  is strongly influenced by stacking registry. In the AA configuration, Mo atoms and chalcogen atoms from opposing layers are vertically aligned, maximizing electron cloud overlap and inducing strong Pauli repulsion. This steric effect pushes the layers apart, resulting in the largest  $c$  values and Mo–Mo interlayer separations ( $d_{\text{int}}$ ), reaching  $6.74 \text{ \AA}$  for homobilayer  $\text{MoS}_2$  and  $6.94 \text{ \AA}$  for  $\text{MoS}_2/\text{MoSe}_2$ . In contrast, the staggered AB and BA configurations allow lateral atomic offsets, reducing localized electronic repulsion and enabling attractive vdW interactions to bring the layers closer to each other. In these registries,  $d_{\text{int}}$  decreases to  $6.43 \text{ \AA}$  for  $\text{MoS}_2$  and  $6.62 \text{ \AA}$  for  $\text{MoS}_2/\text{MoSe}_2$ , with corresponding contractions in  $c$ . The systematic

expansion of approximately 0.20 Å in the heterobilayer relative to the homobilayer reflects the larger vdW radius of Se compared to S.

To characterize the bonding nature and spatial distribution of electrons, the electron localization function (ELF) was analyzed, as illustrated in Fig. 1e–h. ELF values approaching unity indicate regions of strong covalent bonding or lone-pair character, whereas values near zero denote regions of low electron density. Across all configurations, a pronounced low-ELF region ( $\text{ELF} \approx 0$ ) is observed within the interlayer space, identifying the vdW gap and confirming the absence of significant orbital overlap.

The intralayer bonding characteristics are further elucidated by these ELF distributions. In the AB-stacked systems (Fig. 1e,g), the first layer exhibits moderate localization around chalcogen sites, while the second layer shows stronger, more spatially extended localization, indicated by orange-to-red regions. In the BA stacking (Fig. 1f,h), this behavior is inverted, demonstrating a stacking-dependent redistribution of the local electronic environment and highlighting the sensitivity of intralayer charge to the vertical atomic registry.

Interlayer charge redistribution was quantified using charge density difference (CDD) analysis. The three-dimensional CDD isosurfaces, illustrated in Fig. 1i–l, use red and green contours to indicate charge depletion and accumulation, respectively (isovalue =  $0.001 \text{ e}/\text{Å}^3$ ). The CDD,  $\Delta\rho(\mathbf{r})$ , is defined as

$$\Delta\rho(\mathbf{r}) = \rho_{\text{bilayer}}(\mathbf{r}) - \rho_{L_1}(\mathbf{r}) - \rho_{L_2}(\mathbf{r}), \quad (1)$$

where  $\rho_{\text{bilayer}}$ ,  $\rho_{L_1}$ , and  $\rho_{L_2}$  are the charge densities of the bilayer and isolated monolayers at the same atomic coordinates. The planar-averaged redistribution perpendicular to the interface (along the  $z$ -axis) is

$$\Delta\rho(z) = \frac{1}{A} \int \Delta\rho(x, y, z) dx dy, \quad (2)$$

with  $A$  denoting the in-plane unit-cell area. The associated out-of-plane (in stacking direction) dipole moment per unit area is

$$P_z = \frac{1}{A} \int z \Delta\rho(z) dz. \quad (3)$$

The stacking registry dictates the electronic landscape of the bilayers through a competition between structural symmetry and local orbital hybridization. In AA-stacked bilayers, the preservation of an interlayer mirror symmetry plane ( $\sigma_z$ ) enforces a symmetric charge redistribution,  $\Delta\rho(z) = \Delta\rho(-z)$ , fundamentally precluding an out-of-plane dipole ( $P_z = 0$ ). This is corroborated by the symmetry-protected CDD isosurfaces (Fig. S1a,b) and planar-averaged profiles (Fig. S1c,d), which exhibit distributions centered symmetrically across the vdW gap. The vertical alignment of Mo atoms and opposing chalcogen planes in layers L1 and L2 maintains a balanced interlayer hybridization, preserving a non-polar, purely vdW-mediated interaction.

In contrast, the staggered AB and BA registries facilitate a pronounced, asymmetric interlayer charge transfer. For the  $\text{MoS}_2$  homobilayer in the AB configuration (Fig. 1i and Fig. 2a), a spontaneous electronic redistribution occurs, with charge depletion

(holes) localized near the lower layer (L1, red region) and charge accumulation (electrons) concentrated near the top layer (L2, green region). This spatial separation of charge establishes a net upward-oriented electric polarization,  $P_z$  ( $\uparrow$ ). The redistribution originates from the broken global inversion symmetry inherent to staggered registries, which permits asymmetric hybridization between the metal Mo-4 $d_{z^2}$  and chalcogen S-3 $p_z$  orbitals. This effect is quantified by the planar-averaged  $\Delta\rho(z)$ , which exhibits extrema of +0.005 and -0.007 e/ $\text{\AA}^3$ . A structural transition to the BA configuration (Fig. 1j and Fig. 2b) effectively inverts this electronic profile, reversing the dipole orientation to  $P_z$  ( $\downarrow$ ). The existence of these two energetically degenerate states with opposing dipole moments confirms a switchable, bistable interlayer configuration, representing the essential microscopic prerequisite for sliding ferroelectricity in MoS<sub>2</sub> bilayers.

For the chemically asymmetric MoS<sub>2</sub>/MoSe<sub>2</sub> heterobilayer (Fig. 1k,l), a spontaneous electronic redistribution occurs, with charge depletion localized in the MoS<sub>2</sub> layer (L1, red) and charge accumulation in the MoSe<sub>2</sub> layer (L2, green). The magnitude of this interlayer charge transfer is significantly enhanced compared to the homobilayer, as evidenced by the larger absolute range of the CDD values. Despite this increased total charge transfer, the CDD redistribution exhibits a more uniform lateral character, with reduced in-plane modulation across the interface compared to the homobilayer. Both AB and BA stackings display essentially the same distribution, confirming that the intrinsic chemical potential gradient dominates over the geometric registry. This is further supported by the planar-averaged profiles (Fig. 2c,d), which show robust, nearly identical extrema for both configurations, demonstrating that the out-of-plane polarization  $P_z$  ( $\uparrow$ ) is fundamentally pinned by chemical asymmetry rather than being sensitive to relative atomic shifts.

Table 1: Calculated vacuum levels ( $E_{\text{vac}}$ ), work functions ( $\Phi$ ), electronic band gaps ( $E_g$ ) obtained with PBE, PBE+SOC, HSE06, and EVGW<sub>0</sub>@PBE, and photoluminescence (PL) energies of the lowest excitonic transition for bilayer MoS<sub>2</sub> and MoS<sub>2</sub>/MoSe<sub>2</sub> heterobilayers in AB and BA stackings.

System	Stacking	$E_{\text{vac}}$ (eV)	$\Phi$ (eV)	$E_g^{\text{PBE}}$ (eV)	$E_g^{\text{PBE+SOC}}$ (eV)	$E_g^{\text{HSE06}}$ (eV)	$E_g^{\text{EVGW}_0\text{@PBE}}$ (eV)	PL Energy (eV)
Bilayer MoS <sub>2</sub>	AB	4.49	5.10	1.23	1.22	1.74	2.26	2.08
	BA	4.49	5.10	1.25	1.24	1.77	2.29	2.07
MoS <sub>2</sub> /MoSe <sub>2</sub>	AB	4.96	5.30	0.85	0.76	1.24	1.89	1.45
	BA	4.99	5.30	0.75	0.66	1.13	1.78	1.34

The electrostatic consequences of charge redistribution are quantified by the planar-averaged electrostatic potential  $V(z)$ , which is coupled to the charge density difference  $\Delta\rho(z)$  via Poisson's equation:

$$\frac{d^2V(z)}{dz^2} = -\frac{\Delta\rho(z)}{\epsilon_0}. \quad (4)$$

The resulting out-of-plane electric field,  $E_z = -dV/dz$ , is determined by the first

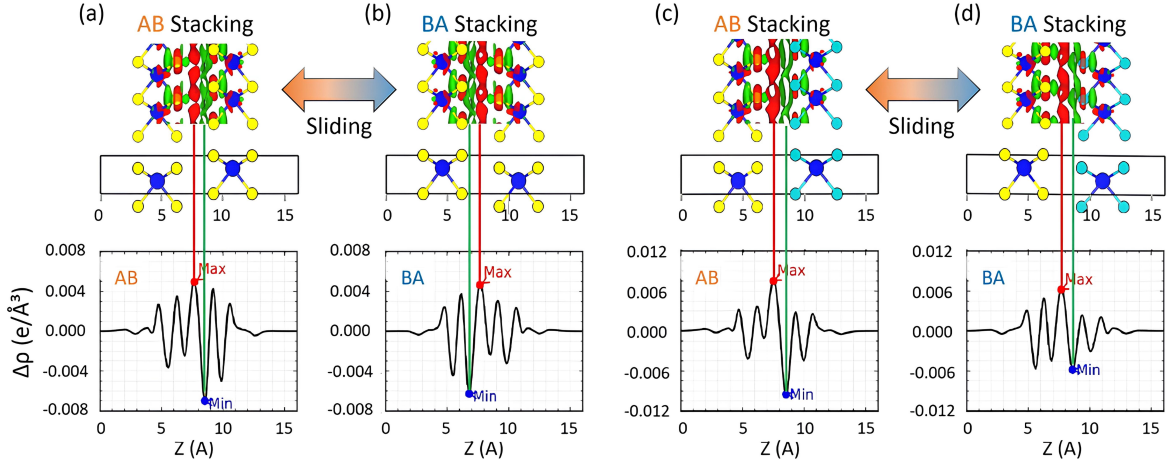


Figure 2: Planar-averaged charge density difference ( $\Delta\rho$ ) profiles for  $\text{MoS}_2$  and  $\text{MoS}_2/\text{MoSe}_2$  bilayers. Panels (a)–(d) display the out-of-plane ( $z$ ) distribution of charge for AB- and BA-stacked configurations. The top insets map the 3D  $\Delta\rho$  isosurfaces to the 1D profiles; red and green vertical lines correlate the quantitative maxima (Max) and minima (Min) with physical regions of electron accumulation and depletion, respectively. The sequence of these extrema (Min $\rightarrow$ Max vs. Max $\rightarrow$ Min) delineates the interfacial dipole orientation, illustrating how lateral sliding between AB and BA stackings reverses or modulates the internal electric field and interlayer coupling.

moment of the redistributed charge. A macroscopic potential shift  $\Delta V$  across the interlayer distance  $d_{\text{int}}$  generates an effective internal field,

$$E_z \approx \frac{\Delta V}{d_{\text{int}}}. \quad (5)$$

For the AB-stacked  $\text{MoS}_2$  homobilayer (Fig. 3a), the planar-averaged potential reveals a distinct layer-to-layer offset of  $\sim 55$  meV. To ensure methodological consistency, we applied a macroscopic averaging technique to filter out periodic variations; this confirms the offset is robust and yields an internal electric field of  $\sim 0.86$  V/nm directed from L2 to L1. Inverting the registry to the BA configuration (Suppl. Mat., Fig. S2a) reverses the sign of the potential difference ( $-55$  meV) and the vector of the internal field. Since the constituent layers are chemically identical, this polarization is an emergent phenomenon driven by registry-induced symmetry breaking and interlayer orbital hybridization.

In contrast, the  $\text{MoS}_2/\text{MoSe}_2$  heterobilayer (Fig. 3b) exhibits a qualitatively distinct electrostatic profile. The planar-averaged potential is dominated by large variations of the peaks ( $\sim 24$  to  $31$  eV) corresponding to the ionic cores of the Se and Mo planes. While these features reflect the intrinsic electronegativity mismatch between S and Se, they represent local atomic-scale variations that do not contribute to a macroscopic dipole. Using the same macroscopic averaging technique applied to the homobilayer, the potential offset for the heterobilayer is found to be negligible (Suppl. Mat., Fig. S2b),

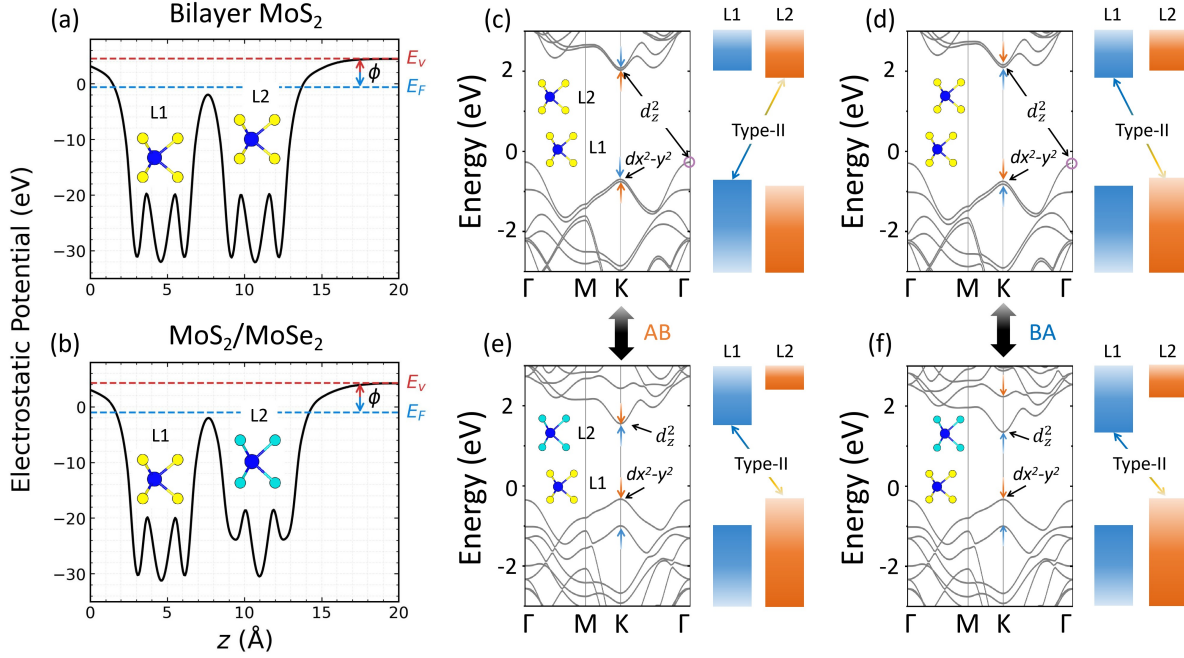


Figure 3: Planar-averaged electrostatic potentials, quasiparticle band structures, and band alignments. (a)–(b) Out-of-plane electrostatic potential profiles for AB-stacked  $\text{MoS}_2$  and  $\text{MoS}_2/\text{MoSe}_2$ , respectively;  $E_v$  and  $\phi$  indicate the vacuum level and work function. (c)–(f) Quasiparticle band structures calculated at the  $\text{EVGW}_0\text{@PBE}$  level for AB and BA stacking orders. The arrows highlight stacking-dependent shifts in the  $d_{z^2}$  and  $d_{x^2-y^2}$  orbitals at the  $K$  point. The right-hand schematics illustrate the resulting Type-II band alignments between layers L1 and L2.

such that:

$$\Delta V_{\text{hetero}} \approx 0, \quad E_z \approx 0. \quad (6)$$

Consequently, despite the pronounced local chemical asymmetry, the  $\text{MoS}_2/\text{MoSe}_2$  interface does not support a stacking-dependent, switchable internal electric field. The intrinsic chemical potential gradient effectively pins the electronic state, suppressing the collective, registry-dependent charge transfer required for the bistable dipolar states observed in the homobilayer.

The calculated vacuum levels and work functions provide a complementary perspective on the electrostatic environment of these layered systems (Table 1). Bilayer  $\text{MoS}_2$  exhibits identical vacuum levels of 4.49 eV for both AB and BA stackings, with corresponding work functions of approximately 5.10 eV, consistent with the presence of a small, reversible interlayer dipole. In contrast, the  $\text{MoS}_2/\text{MoSe}_2$  heterobilayer shows elevated vacuum levels of 4.96 eV (AB) and 4.99 eV (BA), and work functions of  $\sim 5.3$  eV, reflecting the chemical asymmetry of the interface. These values corroborate the electrostatic analysis since the homobilayer supports a bistable, stacking-dependent dipole manifested as the 55 meV potential step, whereas the heterobilayer lacks a

switchable internal field and the macroscopic potential is dominated by intrinsic chemical offsets rather than stacking-induced charge redistribution.

*3.1.2. Stacking-Dependent Electronic Structure and Band Alignment* The electronic properties of homobilayer MoS<sub>2</sub> and MoS<sub>2</sub>/MoSe<sub>2</sub> heterobilayers were evaluated using PBE, PBE+SOC, and HSE06 functionals to investigate the impact of stacking configuration on the band gap  $E_g$  and band-edge localization. To accurately account for many-body effects and the reduced dielectric screening characteristic of two-dimensional systems, eigenvalue-self-consistent quasiparticle calculations were performed within the EVGW<sub>0</sub>@PBE framework. The resulting band gap renormalization and the complex interplay between stacking registry and electronic structure are illustrated in Fig. 3c–f, while a comprehensive comparison across the PBE, PBE+SOC, and HSE06 levels including fully layer- and orbital-resolved band structures is provided in the Suppl. Mat. (Figs. S3–S6).

For the MoS<sub>2</sub> homobilayer, both AB and BA stackings exhibit an indirect  $\Gamma$ – $K$  band gap. At the PBE level, the band gaps are approximately  $E_g \approx 1.23$  eV for AB and 1.25 eV for BA. Including SOC reduces the gaps slightly to about 1.22 eV for AB and 1.24 eV for BA, which is consistent with the moderate spin splitting of the Mo  $d$  states. The HSE06 hybrid functional increases the gaps by roughly 40%, yielding  $E_g \approx 1.71$  eV for AB and 1.74 eV for BA, while EVGW<sub>0</sub>@PBE further enhances them to 2.26 eV for AB and 2.29 eV for BA (Table 1).

This indirect character originates from orbital-selective interlayer hybridization. The VBM and CBM at the  $K$ -point are dominated by in-plane Mo  $d$  orbitals, which suppress interlayer coupling and effectively pin the localized states at  $K$ . Stacking-dependent shifts of these  $d_{z^2}$  and  $d_{x^2-y^2}$  states,  $\Delta_v$  and  $\Delta_c$ , are highlighted by the arrows in Fig. 3c,d, demonstrating how registry modulates local orbital energies. In the AB configuration, the planar-averaged electrostatic potential profile (Fig. 3a) reveals a distinct intrinsic potential offset of  $\sim 55$  meV between the layers, indicating a stacking-dependent dipole. This macroscopic electrostatic environment acts as a perturbation that modifies the electronic states, resulting in band offsets of  $\Delta_v \approx 50$  meV and  $\Delta_c \approx 30$  meV (as derived from the electronic band structure). This relationship is precisely inverted in the BA configuration due to the spatial reversal of the layer symmetry.

The  $\Gamma$ -point valence states are primarily composed of out-of-plane Mo  $d_{z^2}$  and S  $p_z$  orbitals, where the interlayer coupling produces a pronounced bonding–antibonding splitting of  $\Delta_\Gamma = 0.72$  eV (cf. Fig. S4). The electronic coupling at  $\Gamma$  can be estimated using a two-level approximation at the  $\Gamma$ -point. For a homobilayer the uncoupled VBM orbitals are degenerate. However, due to the static electric field there is an offset of  $\Delta = 0.05$  eV as given in the previous subsection. Thus the effective splitting is given by  $\Delta_\Gamma = \sqrt{\Delta^2 + 4t_\Gamma^2}$ . From this expression the coupling (hopping matrix) follows as  $t_\Gamma = 0.36$  eV.

The considerable magnitude of this extracted hopping parameter highlights the

strong interlayer electronic hybridization occurring despite the predominantly vdW nature of the interlayer assembly. This coupling arises from the non-negligible spatial tails of out-of-plane atomic orbitals into the van der Waals gap—which is distinct from covalent bond formation—and this electronic overlap drives the large bonding–antibonding splitting ( $\Delta_\Gamma$ ). This pushes the upper hybridized state above the localized uncoupled states at  $K$ , thereby establishing the definitive indirect band gap character of the homobilayer. Comparing the AB and BA configurations, the negligible variation observed in  $\Delta_\Gamma$  demonstrates that while the local atomic registry directly modulates the layer-dependent potential offset, the interlayer hopping matrix element  $t_\Gamma$  remains fundamentally constrained by the global equilibrium interlayer separation rather than the relative lateral atomic displacement.

As detailed in the quasiparticle band alignment scheme (Suppl. Mat., Fig. S7), these registry-dependent potential offsets ultimately yield a type-II alignment that facilitates the formation of spatially separated interlayer excitons. These are denoted based on their specific interlayer character:  $X_{\text{Ib}}$  (electron localized in the bottom layer),  $X_{\text{It}}$  (electron localized in the top layer), and  $X_{\text{IL}}$  (an exciton state associated with the global lattice registry).

In contrast, the MoS<sub>2</sub>/MoSe<sub>2</sub> heterobilayer exhibits a robust direct type-II band alignment across all staggered registries. The potential profiles in Fig. 3b show large atomic-scale oscillations; while such fluctuations are intrinsic to all van der Waals heterojunctions due to their periodic atomic structure, here they are clearly reflecting the chemical asymmetry between the layers. As depicted in the quasiparticle band structures (Fig. 3e,f), where L1 (MoS<sub>2</sub>, blue) and L2 (MoSe<sub>2</sub>, orange) are color-coded, the CBM is strictly localized on L1, while the VBM resides on L2. This chemical potential mismatch between S and Se effectively overrides the registry-dependent potential shifts, preserving the direct  $K$ – $K$  gap and ensuring that the intrinsic band offsets indicated by the work functions ( $\phi$ ) and vacuum levels ( $E_v$ ) in Fig. 3b remain the primary drivers of electronic localization.

*3.1.3. Optical Properties and Excitonic Response* Excitonic effects were evaluated by solving the Bethe-Salpeter equation (BSE) atop the quasiparticle (QP) landscape (Fig. 4). In these reduced-dimensional systems, the suppressed dielectric screening significantly enhances the electron–hole (e–h) interaction, as evidenced by high exciton binding energies,  $E_b^{\text{exc}} = E_g^{\text{QP}} - E_{\text{opt}}$ , and a substantial renormalization of the absorption onset. The dimensionless oscillator strength quantifies the spectral weight and transition probabilities,  $f_{\text{exc}}$ , defined as:

$$f_{\text{exc}} = \frac{2m_e\omega_{\text{exc}}}{\hbar} |\langle \psi_c | \hat{\mathbf{e}} \cdot \mathbf{r} | \psi_v \rangle|^2, \quad (7)$$

where  $m_e$  is the electron mass,  $\hbar$  is the reduced Planck constant, and  $\omega_{\text{exc}}$  is the excitonic transition frequency. The inclusion of the energy-dependent prefactor ensures that the length units of the position matrix element are properly canceled, yielding the dimensionless values provided by ab initio codes like VASP.

In the MoS<sub>2</sub> homobilayer, the optical response is dominated by robust intralayer excitons with  $f_{\text{exc}} \approx 19$  at 2.085 eV (AB) and 2.073 eV (BA), as shown in Fig. 4a,b and Fig. S8(a,b), respectively. Despite the stacking-induced band offsets,  $\Delta_v$  and  $\Delta_c$ , discussed in the previous section, the negligible energy difference of  $\sim 12$  meV indicates that these intralayer states are largely decoupled from macroscopic interlayer polarization. This stability is consistent with the in-plane  $d_{x^2-y^2}$  and  $d_{xy}$  orbital character of the K-point band edges (Fig. 3c,d), which enforces strong spatial e-h overlap within a single layer and prevents significant interlayer leakage (Fig. 4e,f).

Conversely, the MoS<sub>2</sub>/MoSe<sub>2</sub> heterobilayer exhibits a significantly suppressed oscillator strength,  $f_{\text{exc}} \approx 0$ , for the lowest-energy transitions (Fig. 4c,d). This optical darkness is a direct spectroscopic signature of the intrinsic type-II alignment, where the chemical potential mismatch between S and Se strictly partitions the carriers holes in MoSe<sub>2</sub> and electrons in MoS<sub>2</sub>—yielding a near-zero dipole matrix element. The resulting interlayer excitons ( $X_{\text{Ib}}$ ,  $X_{\text{It}}$ , and  $X_{\text{IL}}$ ; Suppl. Mat., Fig. S7) show pronounced sensitivity to atomic registry, evidenced by a 107 meV stacking-dependent shift, nearly an order of magnitude larger than the variation observed in the homobilayer.

At higher energies ( $\sim 2.45$  eV), hybrid excitonic states emerge with finite oscillator strengths. The observed reduction in hybrid intensity for the BA configuration (cf. Suppl. Mat., Fig. S8(c,d)) relative to the AB configuration (cf. Fig. 4d) correlates with suppressed interlayer orbital hybridization,  $t_{\text{I}}$ , and the modified charge redistribution evident in the CDD profiles (Fig. 2). These results confirm that lateral sliding in TMD heterostructures provides a powerful degree of freedom to modulate the extent of wavefunction delocalization across the van der Waals gap.

### 3.2. Trilayer 2L-MoS<sub>2</sub>/MoSe<sub>2</sub> Heterostructures

#### 3.2.1. Stacking-Dependent Polarization in Trilayer 2L-MoS<sub>2</sub>/MoSe<sub>2</sub> Heterostructures

The evolution of spontaneous out-of-plane polarization was investigated in trilayer heterostructures consisting of a MoSe<sub>2</sub> monolayer atop of a MoS<sub>2</sub> homobilayer (L1-MoS<sub>2</sub>/L2-MoS<sub>2</sub>/L3-MoSe<sub>2</sub>). This 2L-MoS<sub>2</sub>/MoSe<sub>2</sub> architecture introduces additional interlayer degrees of freedom, enabling modulation of the dipole through the interplay of multiple vdW interfaces. High-symmetry stacking sequences (ABA, BAA, ABB, and BAB) are analyzed in Fig. 5a–d, while the asymmetric AAB and BBA configurations are discussed in the Suppl. Mat., Fig. S5.

The in-plane lattice constant  $a$  for all trilayer configurations converges within a narrow range of 3.206–3.208 Å, as summarized in Table S1. This indicates that the observed variations in electronic and polarization properties are primarily driven by registry-dependent interlayer interactions rather than residual epitaxial strain. The out-of-plane lattice parameter  $c$  reflects the stacking-dependent interlayer spacing, with the AAA configuration exhibiting the smallest interlayer contraction (32.19 Å) due to maximal vertical alignment of like-atoms and the resulting Pauli steric repulsion. In contrast, staggered or mixed-symmetry configurations such as ABA, ABB, BAA, BAB,

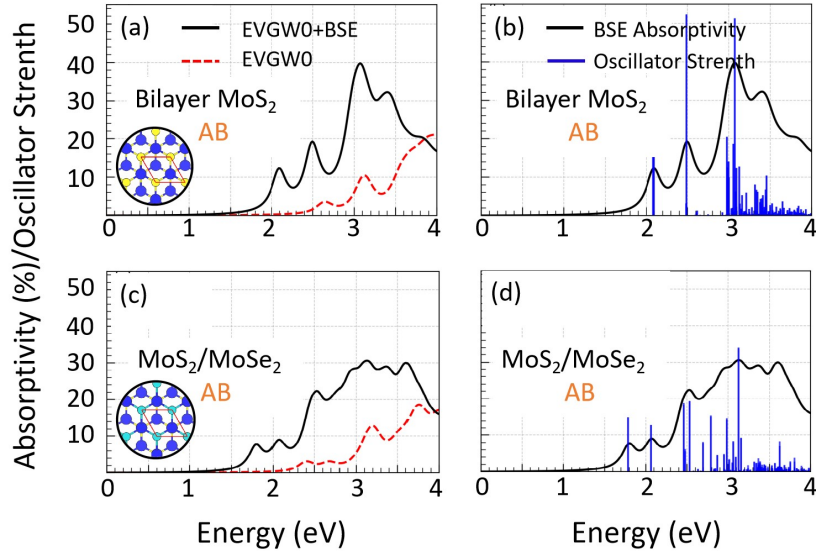


Figure 4: Many-body excitonic absorption spectra and stacking-dependent photoluminescence (PL). (a, c) Absorptivity of AB-stacked bilayer  $\text{MoS}_2$  and  $\text{MoS}_2/\text{MoSe}_2$  calculated at the  $\text{EVGW}_0$  (red dashed) and  $\text{EVGW}_0+\text{BSE}$  (black solid) levels, illustrating the significant excitonic enhancement and band shifts. (b, d) BSE absorptivity (black, broadened with gaussian of width 0.1 eV) with individual transitions and oscillator strengths (blue bars).

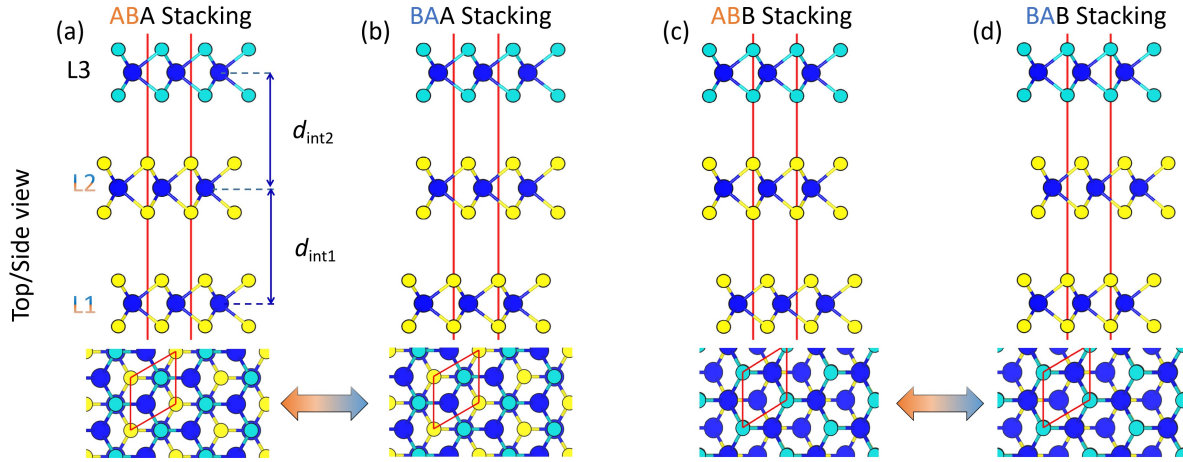


Figure 5: Atomic configurations of 2L- $\text{MoS}_2/\text{MoSe}_2$  heterostructures for different stacking sequences. Panels (a–d) show the ABA, BAA, ABB, and BAB configurations, respectively, in both top and side views. The interlayer distances  $d_{\text{int}1}$  and  $d_{\text{int}2}$  denote the separations between L1–L2 and L2–L3, highlighting the structural variation induced by stacking order.

AAB, and BBA exhibit larger  $c$  values (approximately 36.3–36.5 Å), as the lateral offset between layers reduces steric repulsion and allows vdW attraction to dominate, pulling

the layers closer together.

Side views of the atomic arrangements (Fig. 5a–d) further illustrate the interlayer distances,  $d_{\text{int}1}$  (between L1 and L2) and  $d_{\text{int}2}$  (between L2 and L3), which show strong sensitivity to stacking sequence. For instance,  $d_{\text{int}1}$  contracts to 6.41 Å in ABA and 6.39 Å in BAA relative to AAA (6.70 Å), highlighting the alleviation of Pauli repulsion in staggered registries. This contraction enhances interlayer orbital hybridization, facilitates charge redistribution, and ultimately modulates the net out-of-plane polarization. Table S1 quantitatively captures these trends in  $a$  and  $c$  across all monolayer, bilayer, and trilayer systems, providing a structural framework to rationalize the stacking-dependent electronic and polar properties.

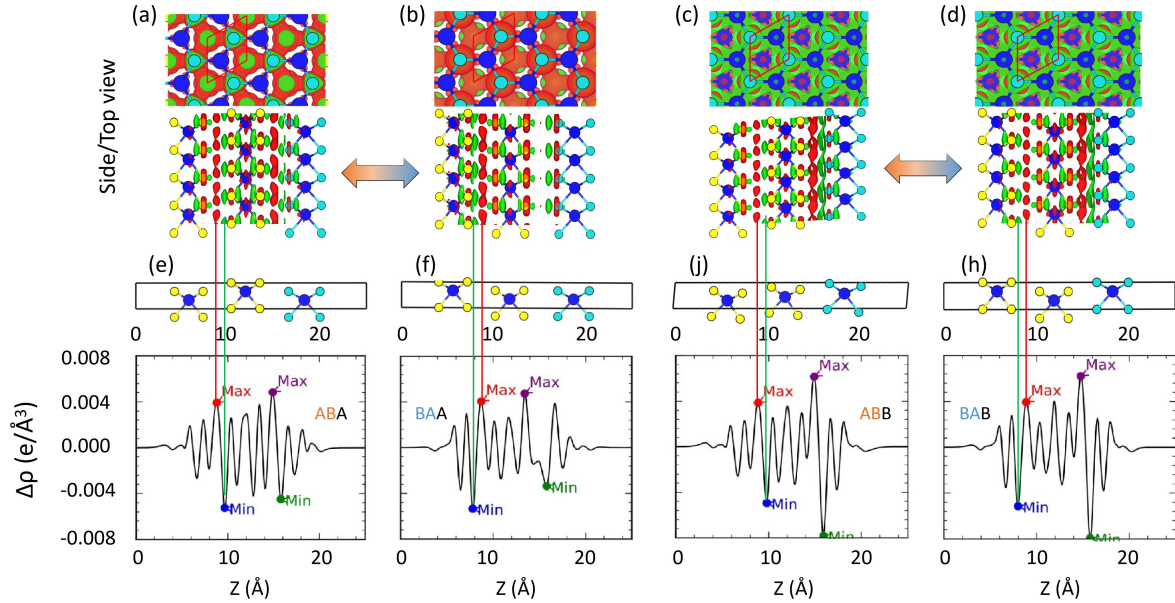


Figure 6: Charge redistribution in 2L- $\text{MoS}_2/\text{MoSe}_2$  heterostructures for different stacking sequences. Panels (a–d) show the charge density difference ( $\Delta\rho$ ) isosurfaces for ABA, BAA, ABB, and BAB configurations, respectively, where yellow and cyan regions represent electron accumulation and depletion (isovalued:  $0.001 \text{ e}/\text{\AA}^3$ ). Panels (e–h) present the corresponding planar-averaged  $\Delta\rho(z)$  profiles across the trilayer, revealing the interfacial dipole characteristics associated with each stacking sequence.

The interlayer charge redistribution was quantified using the planar-averaged CDD

$$\Delta\rho(z) = \rho_{\text{trilayer}}(z) - \sum_{i=1}^3 \rho_{L_i}(z). \quad (8)$$

The 3D isosurfaces and corresponding 1D profiles (Fig. 6a–h) provide a clear spatial map of this redistribution. Analysis of the CDD profiles shows that the L2/L3 ( $\text{MoS}_2/\text{MoSe}_2$ ) interface maintains a robust, stacking-insensitive maximum-to-minimum sequence. This indicates that the interfacial dipole at the heterojunction is primarily dictated by the intrinsic chemical potential mismatch between S and Se, effectively pinning the polarization regardless of the underlying bilayer registry.

In contrast, the L1/L2 ( $\text{MoS}_2/\text{MoS}_2$ ) homobilayer interface acts as a tunable degree of freedom. In the AAA stacking, the L1/L2 junction exhibits a mirror-symmetric charge distribution, yielding a vanishing net dipole (Suppl. Mat., Fig. S9). In ABA and ABB sequences, the L1/L2 interface adopts an AB-type registry, producing a maximum-to-minimum CDD sequence and a corresponding upward dipole vector (Fig. 6e,j). Conversely, BAA and BAB stackings invert this sequence to minimum-to-maximum (Fig. 6f,h), generating a downward dipole vector analogous to BA-type homobilayers.

The AAB and BBA configurations further illustrate the role of structural relaxation in dipole formation. In AAB, the initial AA-like registry of the L1/L2 interface is energetically unstable due to S–S chalcogen repulsion. Subsequent relaxation induces a lateral sliding of L1 toward a BA-like configuration, breaking out-of-plane symmetry and producing a downward dipole. In BBA, the L1/L2 interface occupies a near-equilibrium staggered position, resulting in a symmetric extrema sequence and negligible net polarization (Suppl. Mat., Fig. S10).

Collectively, these results demonstrate that the 2L- $\text{MoS}_2/\text{MoSe}_2$  trilayer behaves as a multistable dipolar system. By delineating the local dipole orientations at each interface whether pointing from the  $\text{MoS}_2$  layers toward  $\text{MoSe}_2$  or in reverse Fig. 6 illustrates how the internal electric field can be significantly modulated.

*3.2.2. Quasiparticle Band Structure Modulation by Stacking in Trilayer 2L- $\text{MoS}_2/\text{MoSe}_2$*  The electronic properties of 2L- $\text{MoS}_2/\text{MoSe}_2$  trilayer heterostructures exhibit a pronounced and systematic sensitivity to atomic registry, as summarized in Table 2, Fig. 7, and Figs. S11–S13. At the PBE+SOC level, the fundamental band gaps span 0.68–0.83 eV, corresponding to a  $\sim 22\%$  modulation driven exclusively by stacking dependent interlayer coupling. This persistence across electronic structure hierarchies identifies atomic registry as an effective internal boundary condition governing the electronic landscape of these quasi-2D heterostructures.

A systematic method comparison reveals consistent changes in the band gap. Moving from PBE to HSE06 increases the band gap by  $\sim 60\text{--}70\%$ , while inclusion of many-body effects at the  $\text{E}^{\text{GW}}_0$ @PBE level introduces a further  $\sim 20\text{--}25\%$  enhancement relative to HSE06 due to quasiparticle renormalization. The resulting quasiparticle gaps (1.51–1.60 eV) exceed PBE+SOC values by  $\sim 110\text{--}120\%$ , reflecting the combined effects of exact exchange and reduced dielectric screening in the layered limit.

The stacking-dependent electronic structure is further illustrated in Fig. 7(a–d), which presents  $\text{E}^{\text{GW}}_0$  band dispersions and type-II alignment schematics for ABA, ABB, BAA, and BAB configurations. Complementary planar-averaged electrostatic potentials  $V(z)$  (Fig. 8(a–d)) reveal that atomic registry imposes a configuration-dependent internal electrostatic field, manifested through systematic shifts in the vacuum level  $E_{\text{vac}}$  relative to the Fermi level  $E_F$ . These shifts directly quantify work-function variations across stackings (5.019 eV for ABA, 5.014 eV for ABB, 4.862 eV for BAA, and 4.975 eV for BAB), establishing electrostatics as a registry-controlled degree

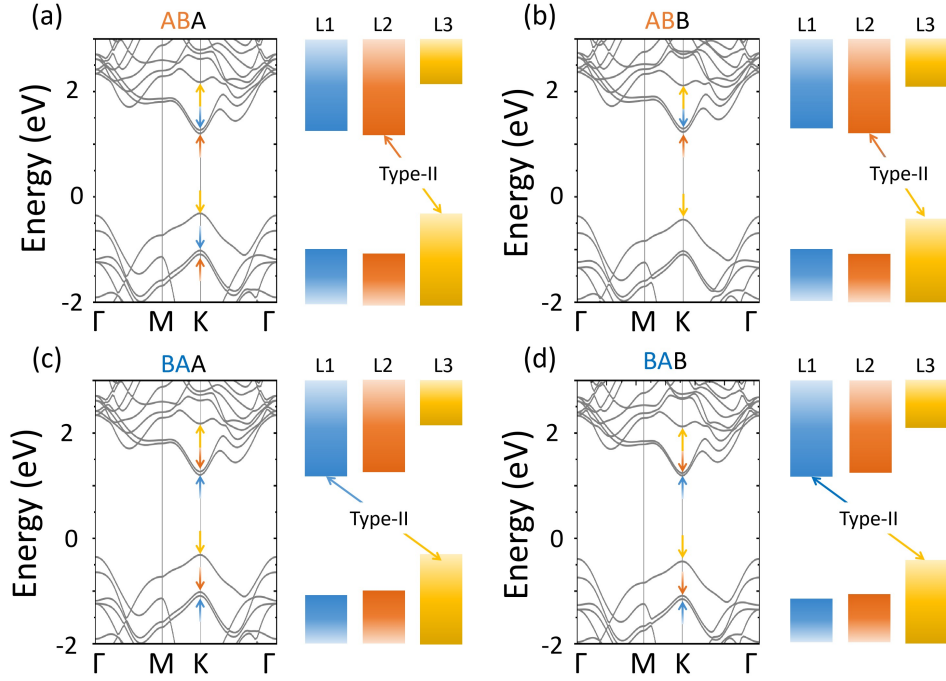


Figure 7: Quasiparticle electronic structures and band alignments of trilayer 2L- $\text{MoS}_2/\text{MoSe}_2$  heterostructures. (a)–(d)  $\text{EVGW}_0$  quasiparticle band structures and corresponding type-II band alignment schematics for ABA, ABB, BAA, and BAB stacking sequences. The arrows at the  $K$  point highlight the stacking-dependent localization of the conduction-band minimum (CBM) and valence-band maximum (VBM) across the L1, L2, and L3 layers.

of freedom.

This registry induced electrostatic landscape originates from stacking dependent structural relaxation at the  $\text{MoS}_2/\text{MoS}_2$  interface, which continuously rebalances Pauli repulsion and van der Waals attraction. The resulting charge redistribution generates asymmetric interfacial dipoles that reshape  $V(z)$ , producing weak but finite internal fields relative to  $E_F$ . Importantly, these fields do not primarily shift absolute band edges; instead, they act as a symmetry-breaking perturbation that competes with interlayer orbital hybridization within the  $\text{MoS}_2$  bilayer, while the  $\text{MoS}_2/\text{MoSe}_2$  interface remains electronically more rigid and serves as a dipolar reference layer.

This competition manifests most strongly in the conduction sector. Layer- and momentum resolved projections at the  $K$  point show that the VBM remains strongly localized on the  $\text{MoSe}_2$  layer across all registries, effectively pinning the valence reference and stabilizing robust type-II alignment. In contrast, the CBM resides in a near-degenerate manifold distributed across the  $\text{MoS}_2$  bilayer, making it highly susceptible to dipole-induced symmetry breaking and interlayer hybridization.

Quantitatively, this is reflected in a systematic reduction of interlayer conduction-band splitting from 62.7–65.8 meV (ABA/ABB) to 53.4–48.5 meV (BAA/BAB),

indicating progressive weakening of internal asymmetry within the MoS<sub>2</sub> bilayer. Crucially, the absolute CBM energy remains nearly invariant across stackings, confirming that registry does not act as a rigid band-edge shift but instead redistributes orbital character within a fixed energetic envelope.

This orbital redistribution is governed by the same electrostatic landscape extracted from  $V(z)$ , where variations in  $E_{\text{vac}} - E_{\text{F}}$  encode the effective work-function modulation. The resulting internal potential bias subtly tunes the balance between delocalizing interlayer hybridization and dipole-induced layer polarization, selectively reshaping the conduction manifold without perturbing the pinned valence reference.

Spin-orbit coupling further refines the band-edge structure at the PBE level, lifting valence-band degeneracies at the  $K$  point and, in selected registries, enhancing direct-gap character. Across all computational levels, the quasiparticle gaps are consistent with experimental photoluminescence trends, with the ABB stacking exhibiting the largest gap and correspondingly strongest optical response.

Overall, stacking registry in 2L-MoS<sub>2</sub>/MoSe<sub>2</sub> trilayers emerges as an internal electrostatic boundary condition that encodes atomic configuration into a self-consistent dipolar landscape. This landscape governs a constrained electronic degree of freedom: a pinned valence manifold coexisting with a dipole-sensitive conduction manifold. The resulting registry electrostatics orbital hierarchy establishes atomic-scale stacking as a deterministic control knob for internal fields, band-edge reconstruction, and optical response in layered heterostructures.

Table 2: Calculated band gaps ( $E_g$ , in eV) using PBE, PBE+SOC, HSE06, and EVGW<sub>0</sub>, along with gap type and photoluminescence (PL) energies for different stacking configurations of 2L-MoS<sub>2</sub>/MoSe<sub>2</sub> trilayer heterostructures. The in-plane lattice constants are reported in Table S1.

Stacking	PBE	PBE+SOC	HSE06	EVGW <sub>0</sub>	PL (eV)	Gap Type
AAA	0.82	0.74	1.25	1.55	1.362	Direct
ABA	0.82	0.73	1.21	1.51	1.287	Direct
ABB	0.86	0.83	1.31	1.60	1.391	Indirect (PBE)/Direct (SOC, HSE06)
BAA	0.77	0.68	1.19	1.51	1.356	Direct
BAB	0.82	0.78	1.28	1.58	1.395	Indirect (PBE)/Direct (SOC, HSE06)
AAB	0.83	0.79	1.28	1.59	1.398	Indirect (PBE)/Direct (SOC, HSE06)
BBA	0.82	0.73	1.22	1.52	1.278	Direct

*3.2.3. Optical Properties and Excitonic Response* The optical response of the 2L-MoS<sub>2</sub>/MoSe<sub>2</sub> trilayer was systematically evaluated to elucidate the impact of stacking-dependent polarization on the many-body excitonic landscape. The specific electronic structure is reflected in the many-body excitonic absorption spectra (Fig. 9a–d), calculated at the EVGW<sub>0</sub>+BSE level using a Gaussian broadening of 0.1 eV. The black solid lines represent the absorption spectra, while the blue bars denote the oscillator strengths ( $f_{\text{exc}}$ ); notably, the absorptivity is the result of the convolution of these

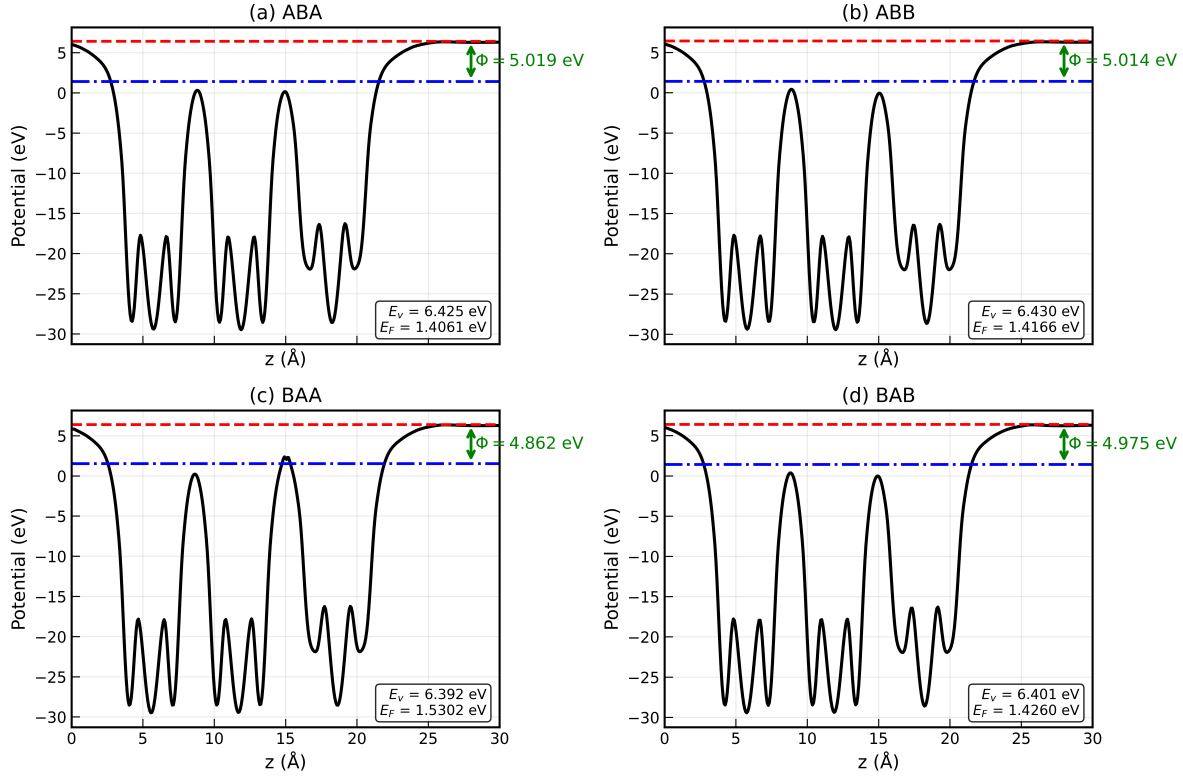


Figure 8: Planar-averaged electrostatic potential profiles  $V(z)$  and work function analysis for trilayer  $2\text{L-MoS}_2/\text{MoSe}_2$  heterostructures. (a)–(d) Potential energy landscapes along the  $c$ -axis for ABA, ABB, BAA, and BAB stackings. Red dashed lines denote the vacuum level ( $E_v$ ), blue dash-dotted lines indicate the Fermi level ( $E_F$ ), and green bidirectional arrows represent the stacking-dependent work function ( $\Phi$ ). The inset information boxes provide the corresponding energetic references obtained after applying a macroscopic averaging filter.

oscillator strengths with the broadening function. For all configurations, the lowest-energy peaks exhibit strongly suppressed oscillator strengths, a hallmark of spatially separated interlayer excitons. The variation in intensity across different stackings reflects differences in interlayer coupling; for example, ABB and BAB configurations exhibit higher oscillator strengths than BAA, indicating enhanced wavefunction overlap across the vdW gap.

Table 2 summarizes the PL energies for the lowest-energy transitions, which span a wide spectral range from 1.278 to 1.398 eV. These variations originate from the interplay between the intrinsic type-II band alignment and stacking-induced electrostatic potential modulations at the  $\text{MoS}_2$  bilayer interfaces (Suppl. Mat., Fig. S7). In these heterostructures, the lowest-energy excitations are dominated by interlayer excitons (ILXs), characterized by spatial separation of charge carriers, with holes localized in the  $\text{MoSe}_2$  valence band and electrons residing in the  $\text{MoS}_2$  bilayer. Consequently, the transition energies are highly sensitive to internal electric fields arising from stacking-

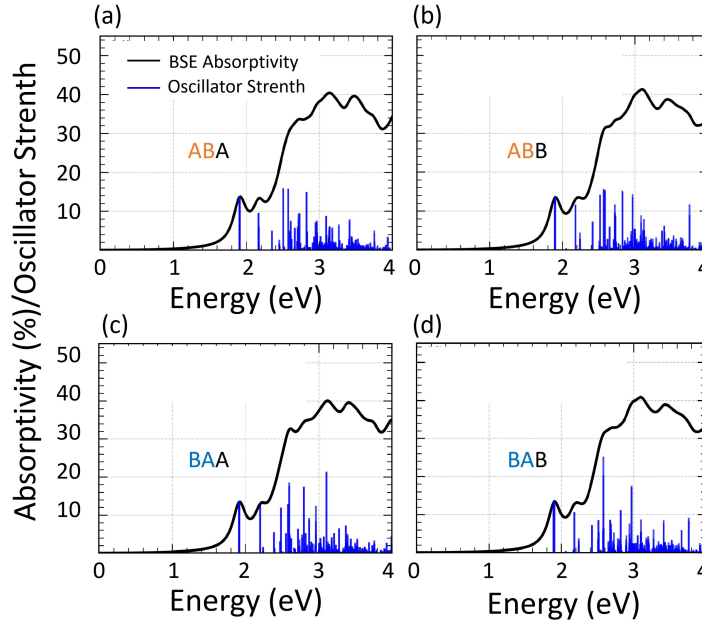


Figure 9: Excitonic absorption of trilayer 2L- $\text{MoS}_2/\text{MoSe}_2$  heterostructures.(e)–(h) Many-body excitonic absorption spectra (black solid lines, Gaussian broadening with width 0.1 eV) and oscillator strengths (blue bars) calculated at the  $\text{EVGW}_0+\text{BSE}$  level. The variations in the low-energy excitonic peaks reflect the modulation of interlayer coupling and spatial charge separation induced by the different stacking registries.

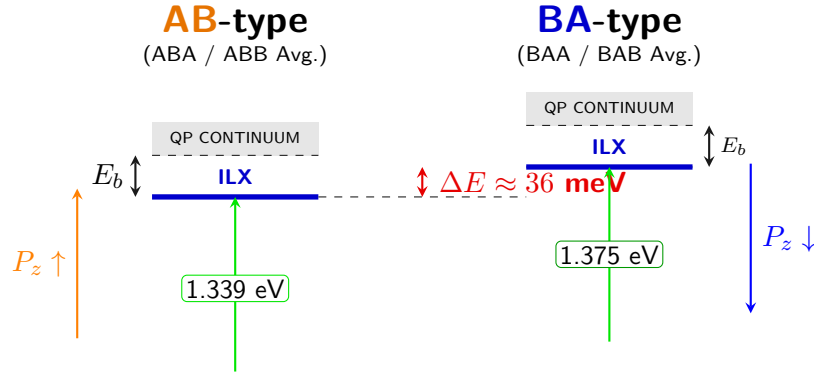


Figure 10: Schematic representation of the energy level shifts for ILXs in AB- and BA-type stackings. Energy levels are based on  $\text{EVGW}_0 + \text{BSE}$  calculations. The  $\Delta E \approx 36 \text{ meV}$  shift represents the calculated registry-dependent offset; experimental PL energies, which represent ensemble averages, are found to be consistent with this framework.[29]

dependent dipole moments. This can already be seen from the  $\text{EVGW}_0+\text{BSE}$  absorption spectra (Fig. 9a–d) where AB-type stackings (ABA and ABB) exhibit stronger excitonic peaks compared to BA-type configurations (BAA and BAB), reflecting enhanced electron–hole wavefunction overlap.

To quantitatively assess the effect of polarization reversal, the average ILX energies for the two stacking families were evaluated. This approximately accounts for variable stacking configurations between  $\text{MoS}_2$  and  $\text{MoSe}_2$  due to lattice mismatch and domain disorder in actual experiments. For AB-type configurations, the characteristic energy is defined as  $E_{\text{AB}}^{\text{avg}} = (E_{\text{ABA}} + E_{\text{ABB}})/2 \approx 1.339$  eV, whereas for BA-type configurations it is given by  $E_{\text{BA}}^{\text{avg}} = (E_{\text{BAA}} + E_{\text{BAB}})/2 \approx 1.375$  eV. This results in an interlayer excitonic energy shift  $\Delta E_{\text{ILX}} = E_{\text{BA}}^{\text{avg}} - E_{\text{AB}}^{\text{avg}} \approx 36$  meV.

The microscopic origin of this shift is schematically illustrated in Fig. 10. In the AB-type stacking, the internal polarization establishes a reference electrostatic potential landscape for ILX formation. Upon switching to the BA-type configuration, the reversal of the out-of-plane dipole ( $P_z$ ) induces a nearly rigid shift of the electrostatic potential across the layers. Importantly, this shift affects both the conduction- and valence-band edges in a similar manner, leaving the exciton binding energy largely unchanged while translating the ILX transition energy to higher values by  $\sim 36$  meV. This behavior can be interpreted as an intrinsic electrostatic gating effect driven by stacking-controlled polarization.

The predicted shift of 36 meV is in excellent agreement with the experimentally reported value of approximately 40 meV [29], confirming that stacking-governed internal dipoles are the dominant mechanism for excitonic energy tuning. The remaining discrepancy ( $\sim 10\%$ ) is likely attributable to additional dielectric screening effects, such as hBN encapsulation in experimental samples, which are not explicitly included in the present calculations.

Finally, the full range of spectral tunability reaches 108 meV between the ABA and BAB configurations, demonstrating that the trilayer architecture significantly expands the accessible energy landscape compared to conventional bilayers. By switching the stacking registry between AB- and BA-type configurations, discrete and reversible shifts in ILX emission energy can be achieved, effectively stabilizing excitons at distinct energy levels.

#### 4. Conclusion

In summary, this work provides a comprehensive investigation of the stacking-dependent electronic and excitonic landscapes in  $\text{MoS}_2$ -based vdW heterostructures. By employing eigenvalue-self-consistent  $GW_0$  calculations combined with the Bethe-Salpeter equation ( $GW+BSE$ ), we elucidate the fundamental mechanisms by which atomic registry governs interfacial polarization and quasiparticle band alignments.

Our analysis of the  $\text{MoS}_2$  homobilayer demonstrates that lateral sliding between AB and BA registries enables a reversible inversion of the out-of-plane dipole moment. This switchability, driven by registry-induced symmetry breaking and asymmetric orbital hybridization, establishes the microscopic foundation for sliding ferroelectricity. In contrast, the  $\text{MoS}_2/\text{MoSe}_2$  heterobilayer exhibits a robust, non-switchable polarization pinned by the intrinsic chemical potential mismatch between sulfur and selenium, which

effectively overrides the geometric registry and stabilizes a type-II band alignment.

In trilayer 2L-MoS<sub>2</sub>/MoSe<sub>2</sub> configurations, an expanded parameter space for deterministic control of charge carriers emerges. The stacking sequence dictates whether photogenerated electrons are localized in the central or bottom MoS<sub>2</sub> layer, while holes remain confined to the MoSe<sub>2</sub> monolayer. This layer-selective behavior can be described within an electrostatic framework, where internal electric fields induce band-edge shifts of 60–70 meV, directly linking dipole orientation to electronic localization.

The many-body excitonic spectra further corroborate these findings. Interlayer excitons exhibit strong sensitivity to atomic registry, with stacking-dependent energy shifts reaching up to 108 meV. Notably, the calculated average interlayer excitonic shift of 36 meV shows excellent agreement with the experimentally reported ~40 meV ferroelectric shift in 3R-MoS<sub>2</sub>/MoSe<sub>2</sub> heterostructures. This quantitative agreement confirms that stacking-governed internal dipoles are the primary drivers of excitonic tunability.

Overall, these results demonstrate that the interplay between structural sliding and many-body interactions in TMD trilayers provides a powerful degree of freedom for engineering programmable light–matter interactions. The ability to modulate excitonic energies and carrier transfer pathways through precise control of stacking sequence offers a promising route toward multi-state optoelectronic memory and next-generation sliding ferroelectric devices.

## Acknowledgments

This work was funded by the Deutsche Forschungsgemeinschaft (DFG, German Research Foundation) - SFB 1477 "Light-Matter Interactions at Interfaces", project number 441234705".

## References

- [1] Zhao K, He D, Fu S, Bai Z, Miao Q, Huang M, Wang Y and Zhang X 2022 *Nanomaterials* **12** 3418
- [2] Xue F, He J H and Zhang X 2021 *Applied Physics Reviews* **8** 021316
- [3] Vizner Stern M, Waschitz Y, Cao W, Nevo I, Watanabe K, Taniguchi T, Sela E, Urbakh M, Hod O and Ben Shalom M 2021 *Science* **372** 1462–1466
- [4] Chen X, Xuan X, Guo W and Zhang Z 2025 *npj 2D Materials and Applications* **9** 10
- [5] Niu Y, Li L, Qi Z, Aung H H, Han X, Tenne R, Yao Y, Zak A and Guo Y 2023 *Nature Communications* **14** 5578
- [6] Li S, Wei K, Liu Q, Tang Y and Jiang T 2024 *Frontiers of Physics* **19** 42501
- [7] Tran K, Choi J and Singh A 2021 *2D Materials* **8** 022002
- [8] Amin B, Singh N and Schwingenschlögl U 2015 *Physical Review B* **92** 075439

- [9] Berkelbach T C, Hybertsen M S and Reichman D R 2013 *Physical Review B* **88** 045318
- [10] Mak K F, Lee C, Hone J, Shan J and Heinz T F 2010 *Physical Review Letters* **105** 136805
- [11] Wang F, Wang J, Guo S, Zhang J, Hu Z and Chu J 2017 *Scientific Reports* **7** 44712
- [12] Xiao D, Liu G B, Feng W, Xu X and Yao W 2012 *Physical Review Letters* **108** 196802
- [13] Wang G, Chernikov A, Glazov M M, Heinz T F, Marie X, Amand T and Urbaszek B 2018 *Reviews of Modern Physics* **90** 021001
- [14] Hong X, Kim J, Shi S F, Zhang Y, Jin C, Sun Y, Tongay S, Wu J, Zhang Y and Wang F 2014 *Nature Nanotechnology* **9** 682–686
- [15] Ceballos F, Bellus M Z, Chiu H Y and Zhao H 2014 *ACS Nano* **8** 12717–12724
- [16] Tran K, Moody G, Wu F, Lu X, Choi J and Li X 2019 *Nature* **567** 71–75
- [17] Zhang N, Surrente A, Baranowski M, Maude D K, Gant P C, Castellanos-Gomez A and Plochocka P 2018 *Nano Letters* **18** 7651–7657
- [18] Choi J, Florian M, Steinhoff A, Erben D, Tran K, Kim D S and Li X 2021 *Physical Review Letters* **126** 047401
- [19] Jiang Y, Chen S, Zheng W and Pan A 2021 *Light: Science & Applications* **10** 72
- [20] Li S, Wei K, Liu Q, Tang Y and Jiang T 2024 *Frontiers of Physics* **19** 42501
- [21] Jung E, Park J C, Seo Y S, Kim J H, Hwang J and Lee Y H 2022 *Scientific Reports* **12** 4543
- [22] Lin Q, Fang H, Kalaboukhov A, Liu Y, Zhang Y, Fischer M, Li J, Hagel J, Brem S, Malic E, Stenger N, Sun Z, Wubs M and Xiao S 2024 *Nature Communications* **15** 8762
- [23] Zhang Q, Fan A, Wang Y, Wu F, Li L, Meng H and Geng D 2025 *npj 2D Materials and Applications* **9** 76
- [24] Cao W, Hod O and Urbakh M 2022 *ACS Applied Materials & Interfaces* **14** 57492–57499
- [25] Pan J, Wang H, Zou L, Wang X, Zhang L, Dong X, Xie H B, Ding Y, Zhang Y, Watanabe K, Taniguchi T, Wang S and Wang Z 2025 *Physical Review Letters* **135** 126603
- [26] Yang D, Liang J, Wu J and Ye Z 2024 *Nature Communications* **15** 1389
- [27] Jiang Y, Chen S, Zheng W, Zheng B and Pan A 2021 *Light: Science & Applications* **10** 72
- [28] Hou S, Xie X, Li S, Chen J, Zhang X and Liu Y 2025 *ACS Nano* **19** 34954–34965
- [29] Schwandt-Krause J, Miloudi M E A, Blundo E, Deb S, Heidkamp J N, Watanabe K, Taniguchi T and Korn T 2026 *Nano Letters* **26** 214–221
- [30] Blöchl P E 1994 *Physical Review B* **50** 17953–17979

- [31] Kresse G and Joubert D 1999 *Physical Review B* **59** 1758–1775
- [32] Kresse G and Furthmüller J 1996 *Physical Review B* **54** 11169–11186
- [33] Kresse G and Furthmüller J 1996 *Computational Materials Science* **6** 15–50
- [34] Perdew J P, Burke K and Ernzerhof M 1996 *Physical Review Letters* **77** 3865–3868
- [35] Hybertsen M S and Louie S G 1986 *Physical Review B* **34** 5390–5413
- [36] Wilhelm J, Seewald P and Golze D 2021 *Journal of Chemical Theory and Computation* **17** 1662–1677
- [37] Hanke W and Sham L J 1980 *Physical Review B* **21** 4656–4673
- [38] Strinati G 1988 *Rivista del Nuovo Cimento* **11** 1–86

# Supporting Material: Stacking-Directed Polarization and Excitonic Engineering in MoS<sub>2</sub>/MoSe<sub>2</sub> van der Waals Heterostructures

Mohammed El Amine Miloudi and Oliver Kühn

*Institute of Physics, University of Rostock, Rostock, Germany*

## CONTENTS

- Bilayer charge density differences and structures (Fig. S1)
- Bilayer electrostatic potentials (Fig. S2)
- Bilayer band structures (Figs. S3–S6)
- Excitonic alignment scheme (Fig. S7)
- Bilayer absorption spectra (Fig. S8)
- Trilayer charge density difference (Fig. S9-S10)
- Trilayer band structures (Figs. S11–S13)

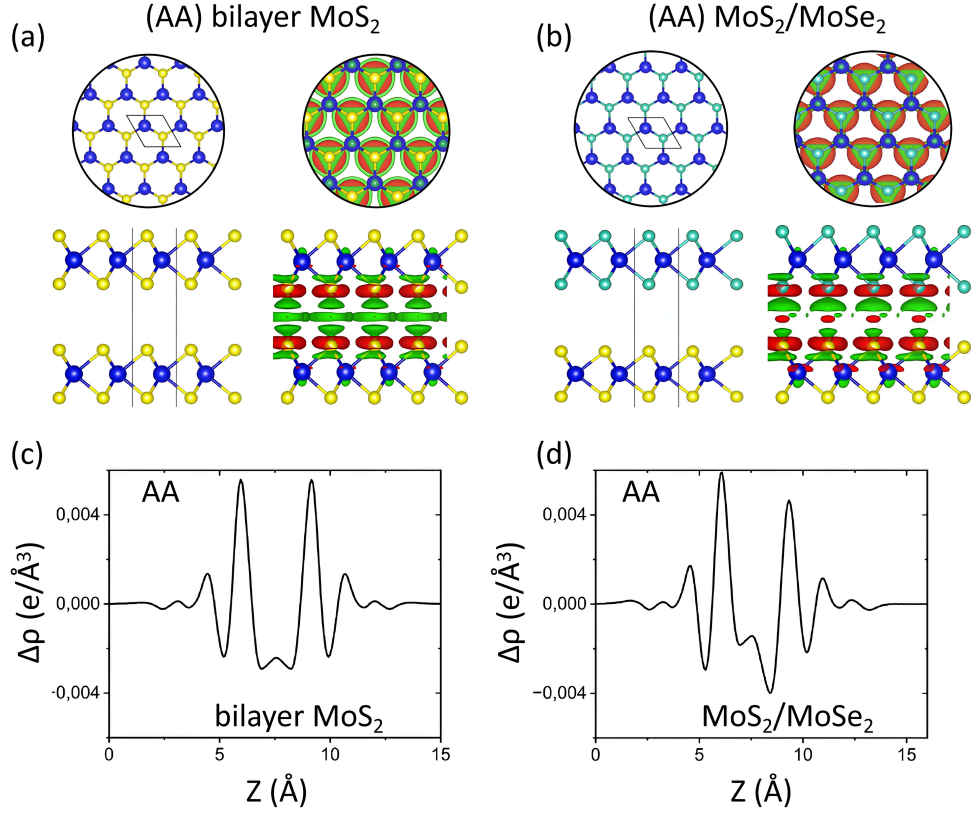


FIG. S1: (a, b) Top and side views of the AA-stacked bilayer MoS<sub>2</sub> (a) and the MoS<sub>2</sub>/MoSe<sub>2</sub> heterobilayer (b), along with their corresponding charge density difference (CDD) isosurfaces. (c, d) Planar-averaged CDD profiles for the bilayer MoS<sub>2</sub> (c) and MoS<sub>2</sub>/MoSe<sub>2</sub> heterobilayer (d). Red and green indicate charge depletion and accumulation, respectively.

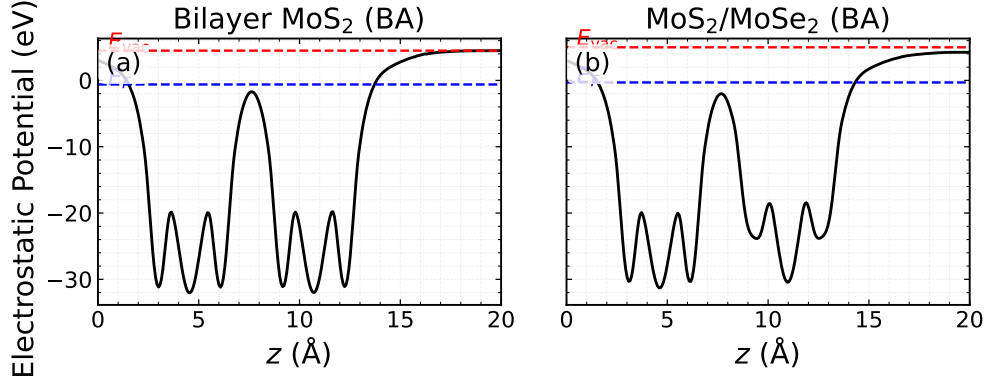


FIG. S2: (a, b) Planar-averaged electrostatic potential profiles of the BA-stacked bilayer MoS<sub>2</sub> (a) and the MoS<sub>2</sub>/MoSe<sub>2</sub> heterobilayer (b). The work function is obtained from the difference between vacuum and Fermi levels.

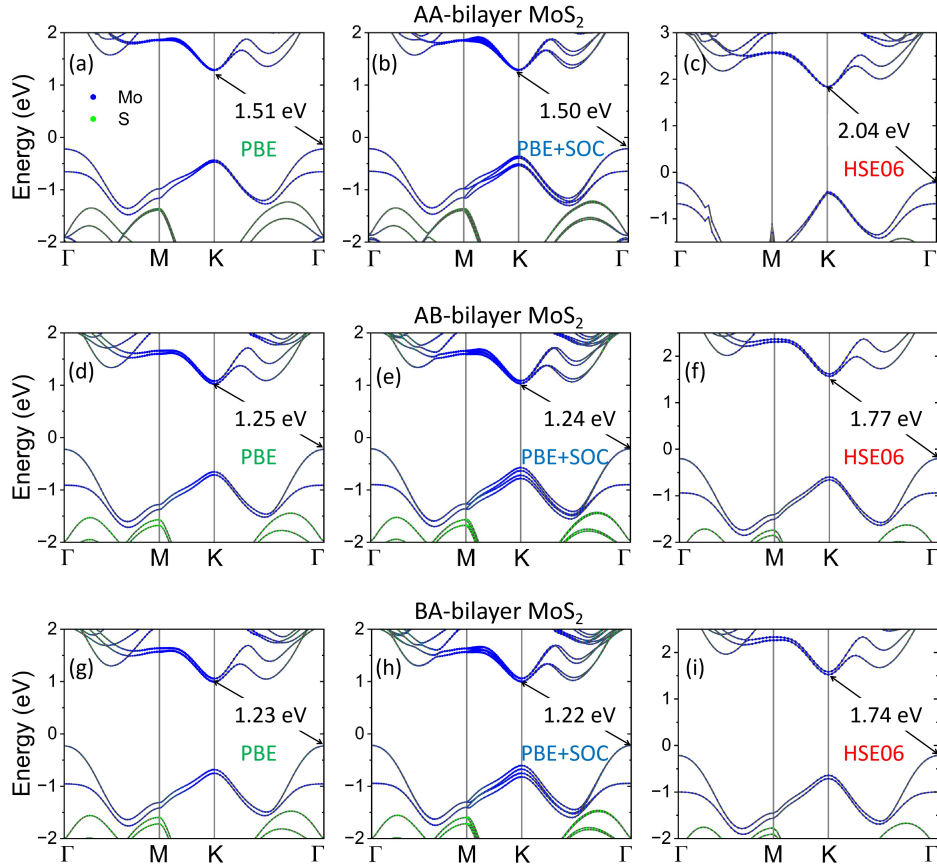


FIG. S3: Projected electronic band structures of AA-, AB-, and BA-stacked bilayer MoS<sub>2</sub> calculated with PBE, PBE+SOC, and HSE06.

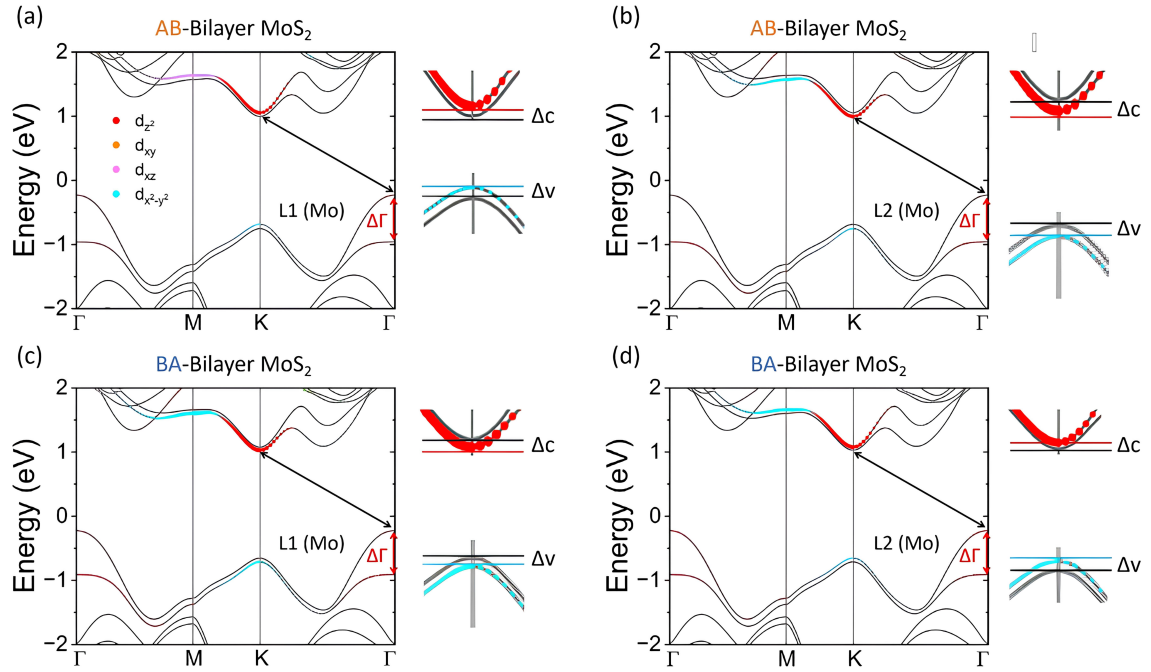


FIG. S4: Spin- and orbital-resolved PBE band structures of bilayer MoS<sub>2</sub> for AB and BA stacking, showing layer-resolved contributions and type-II band alignment.

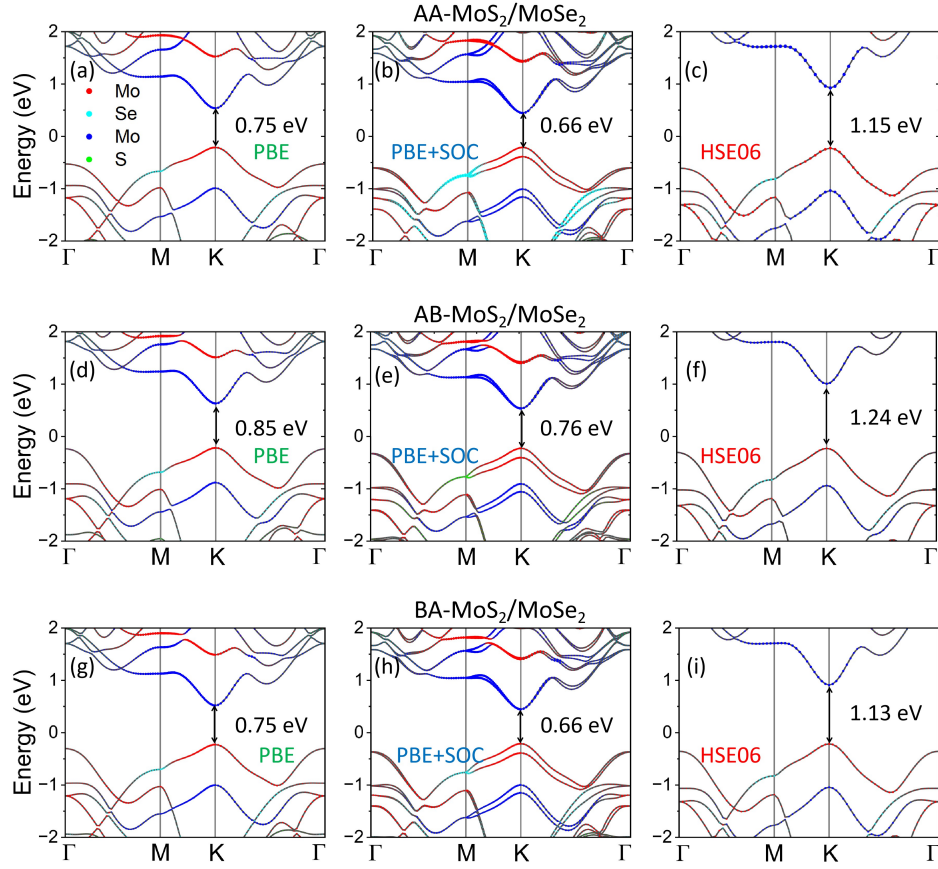


FIG. S5: Projected electronic band structures of AA-, AB-, and BA-stacked  $\text{MoS}_2/\text{MoSe}_2$  heterobilayers.

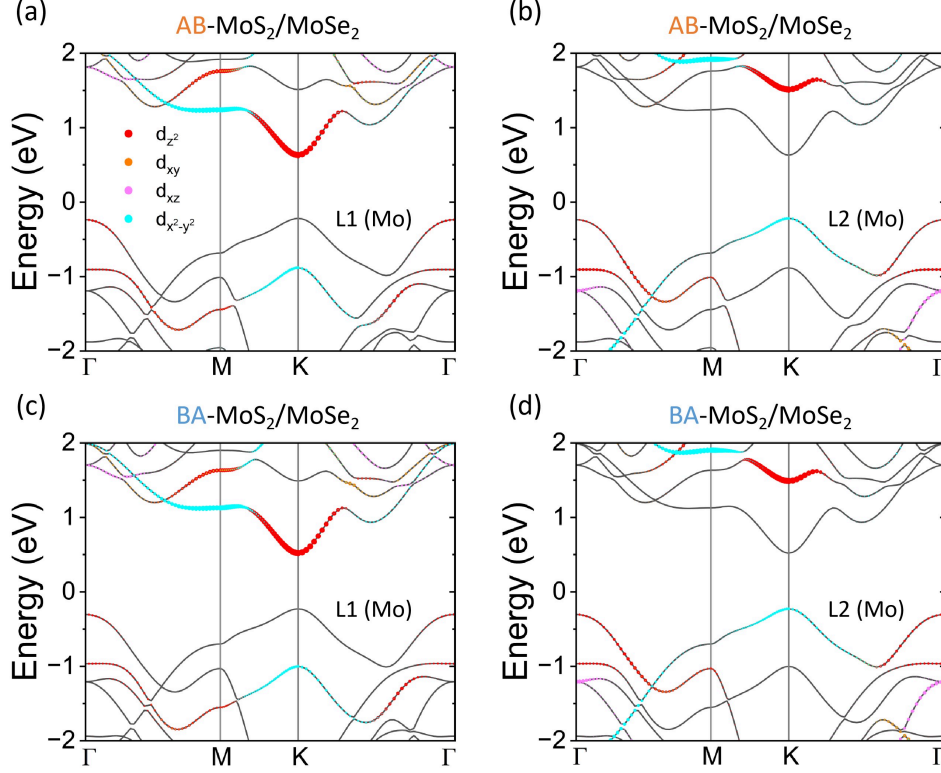


FIG. S6: Spin- and orbital-resolved PBE band structures of the  $\text{MoS}_2/\text{MoSe}_2$  heterobilayer for AB and BA stacking. Panels (a,b) correspond to the AB-stacked heterobilayer for layer 1 (L1 =  $\text{MoS}_2$ ) and layer 2 (L2 =  $\text{MoSe}_2$ ), showing contributions from Mo  $d_{z^2}$ ,  $d_{xy}$ ,  $d_{x^2-y^2}$ , and  $d_{xz}$  orbitals and the layer-resolved localization of the valence-band maximum (VBM) and conduction-band minimum (CBM). Panels (c,d) show the BA-stacked heterobilayer, illustrating the stacking-induced redistribution of band-edge states while preserving the direct-gap character at  $K$ . These results confirm type-II band alignment, with the VBM predominantly localized on  $\text{MoSe}_2$  and the CBM on  $\text{MoS}_2$ . Consistent layer-dependent band alignment is obtained using HSE06 and  $\text{EV}G_0W_0$  calculations.

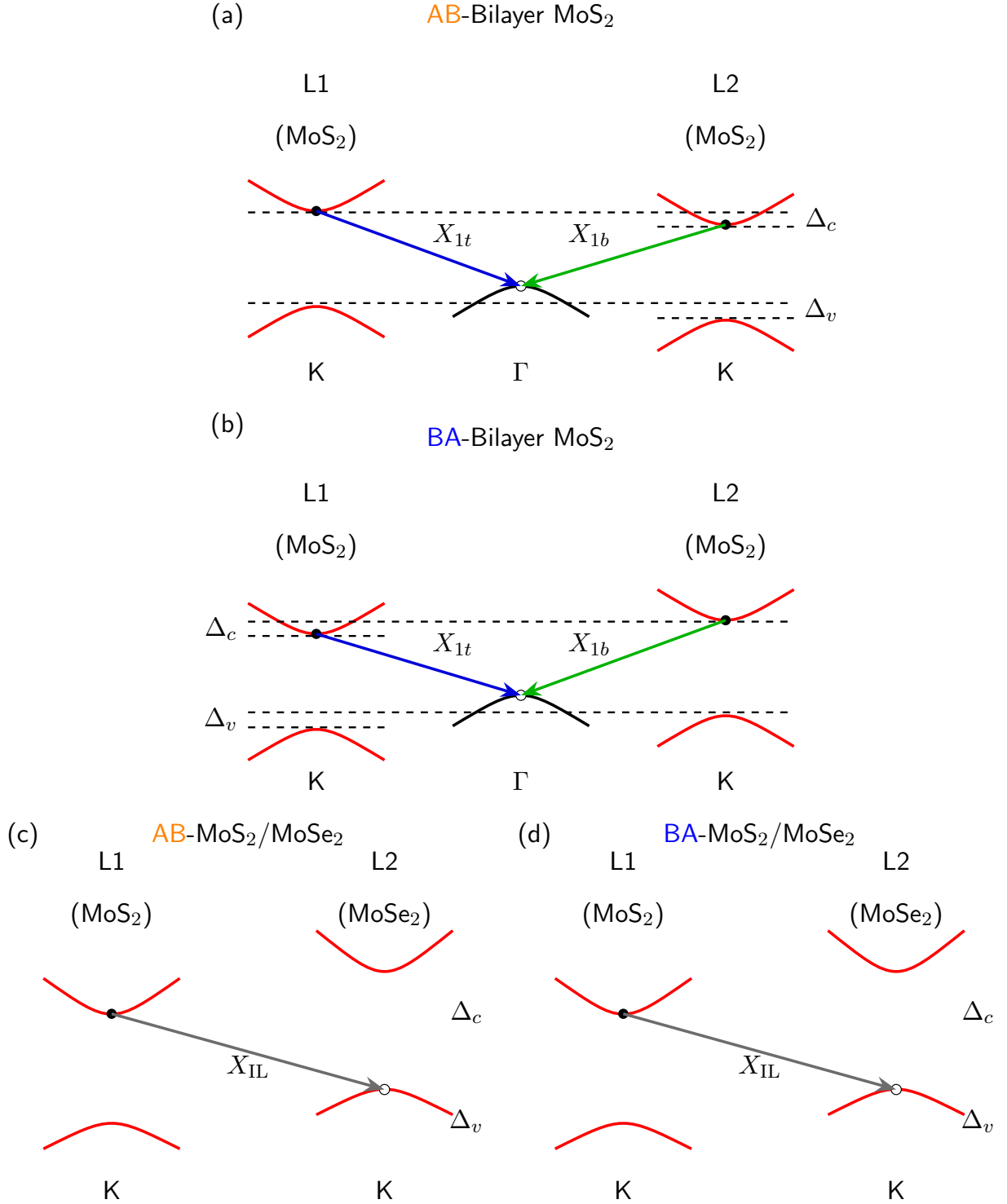


FIG. S7: Quasiparticle band alignment and interlayer  $\Gamma$ - $K$  excitons in AB- and BA-stacked bilayer MoS<sub>2</sub> and MoS<sub>2</sub>/MoSe<sub>2</sub>. Layer-dependent VBM and CBM offsets ( $\Delta_v \approx 50$  meV,  $\Delta_c \approx 30$  meV) result in type-II alignment and spatially separated interlayer excitons  $X_{1b}$ ,  $X_{1t}$ , and  $X_{IL}$ .

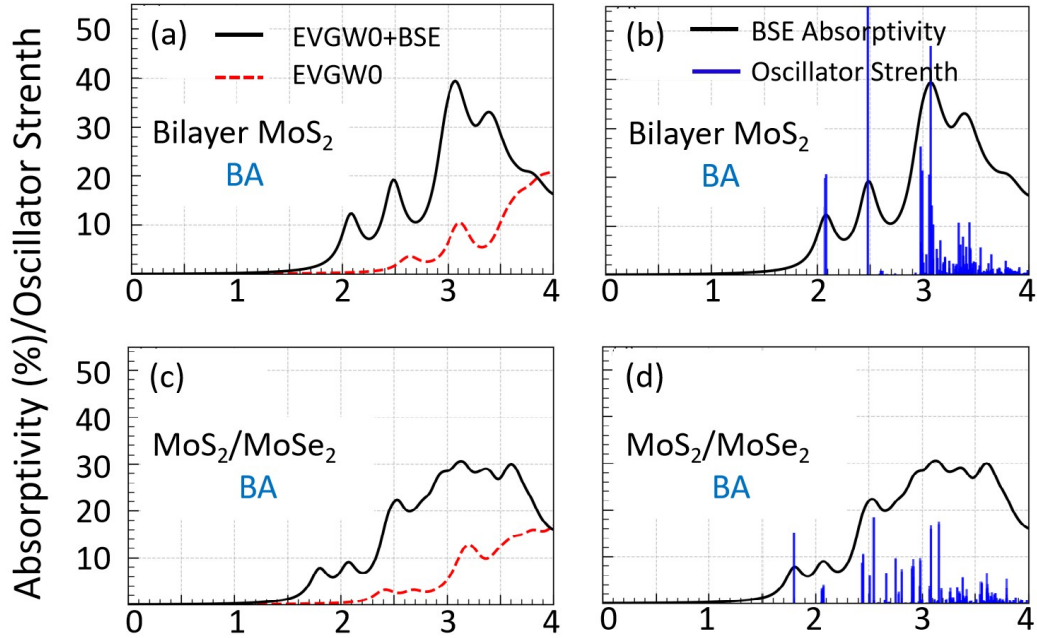


FIG. S8: Many-body excitonic absorption spectra and stacking-dependent photoluminescence (PL). (a, c) Absorptivity of BA-stacked bilayer MoS<sub>2</sub> and MoS<sub>2</sub>/MoSe<sub>2</sub> calculated at the EVGW<sub>0</sub> (red dashed) and EVGW<sub>0</sub>+BSE (black solid) levels, illustrating the significant excitonic enhancement and band shifts. (b, d) BSE absorptivity (black, broadened) with individual transitions and oscillator strengths (blue bars).

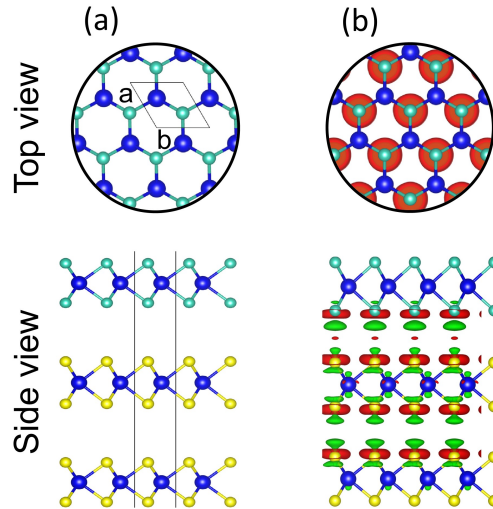


FIG. S9: Top and side views of the trilayer 2L-MoS<sub>2</sub>/MoSe<sub>2</sub> heterostructure with AAA stacking (a,b), together with the corresponding charge density difference (CDD) isosurfaces.

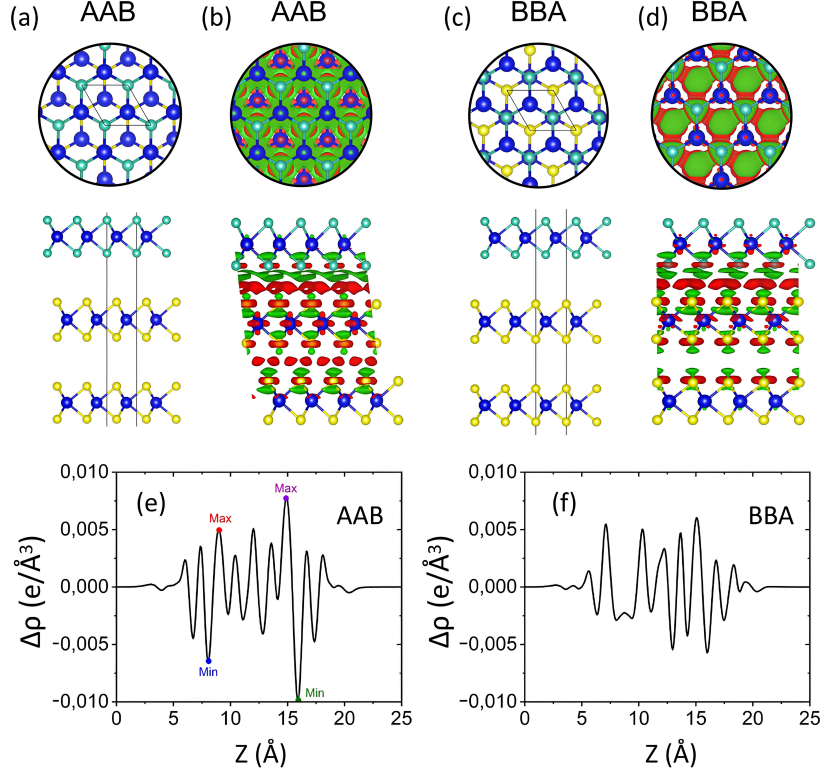


FIG. S10: (a, b) Top and side views of the trilayer 2L-MoS<sub>2</sub>/MoSe<sub>2</sub> heterostructure with AAB stacking, and (c, d) those with BBA stacking, along with their corresponding charge density difference (CDD) isosurfaces. (e, f) Planar-averaged CDD profiles for the AAB (e) and BBA (f) configurations. Red and green indicate charge depletion and accumulation, respectively.

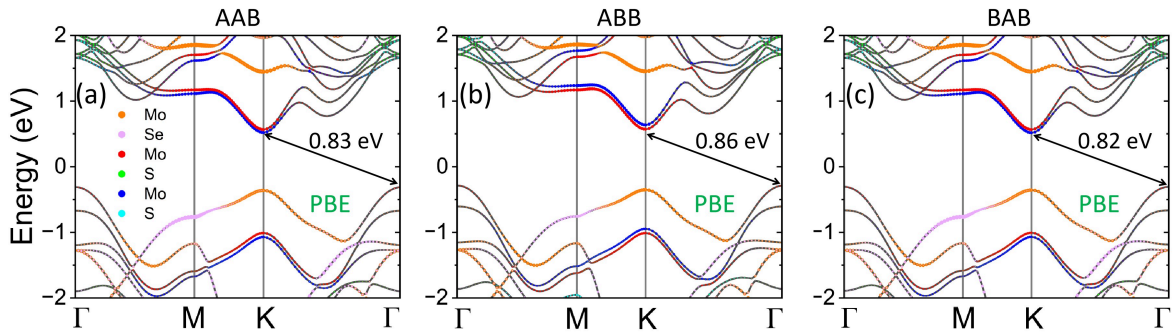


FIG. S11: Electronic band structures of trilayer heterostructures (AAB, ABB, BAB) at the PBE level.

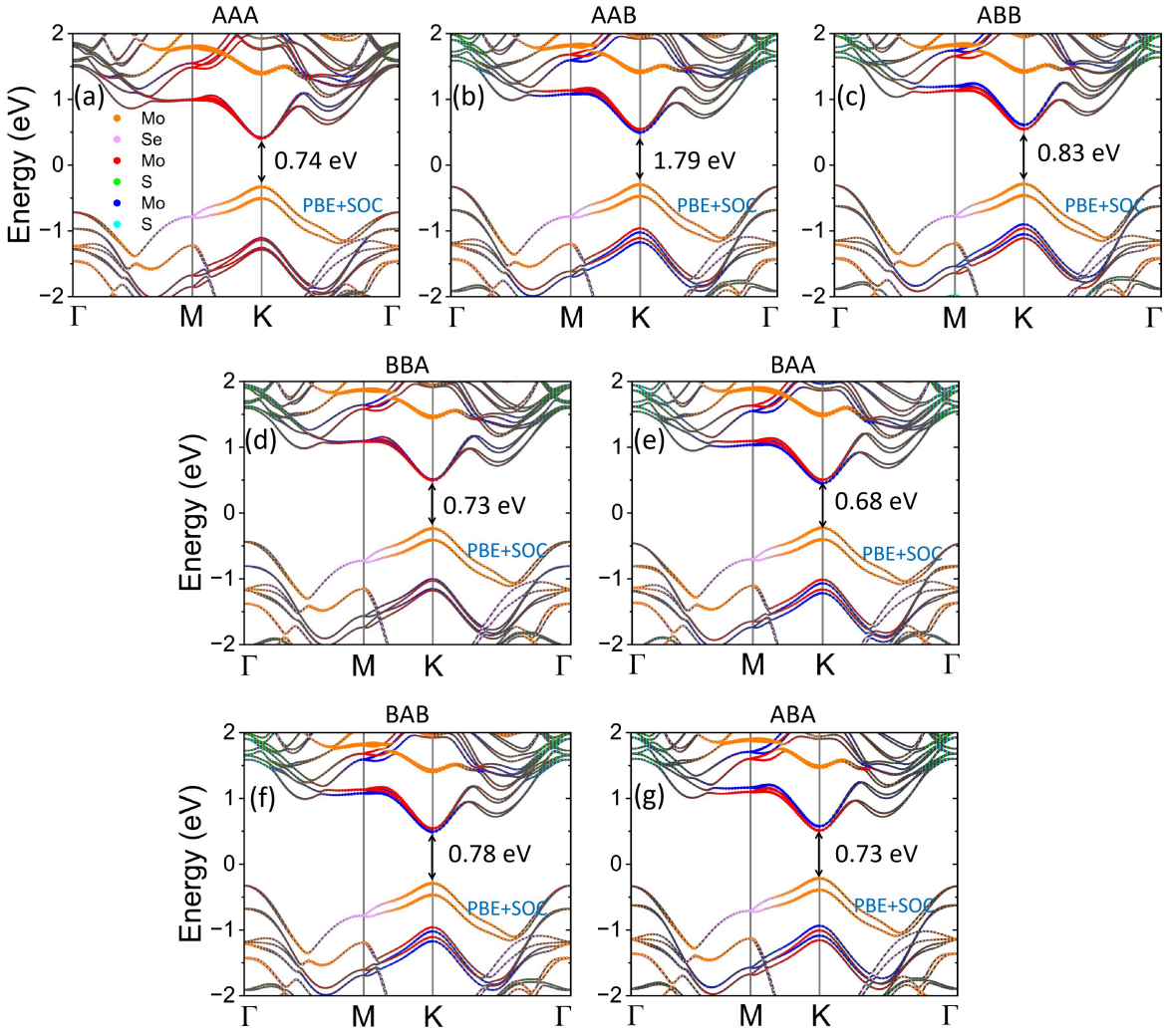


FIG. S12: Electronic band structures including spin-orbit coupling for all stacking configurations.

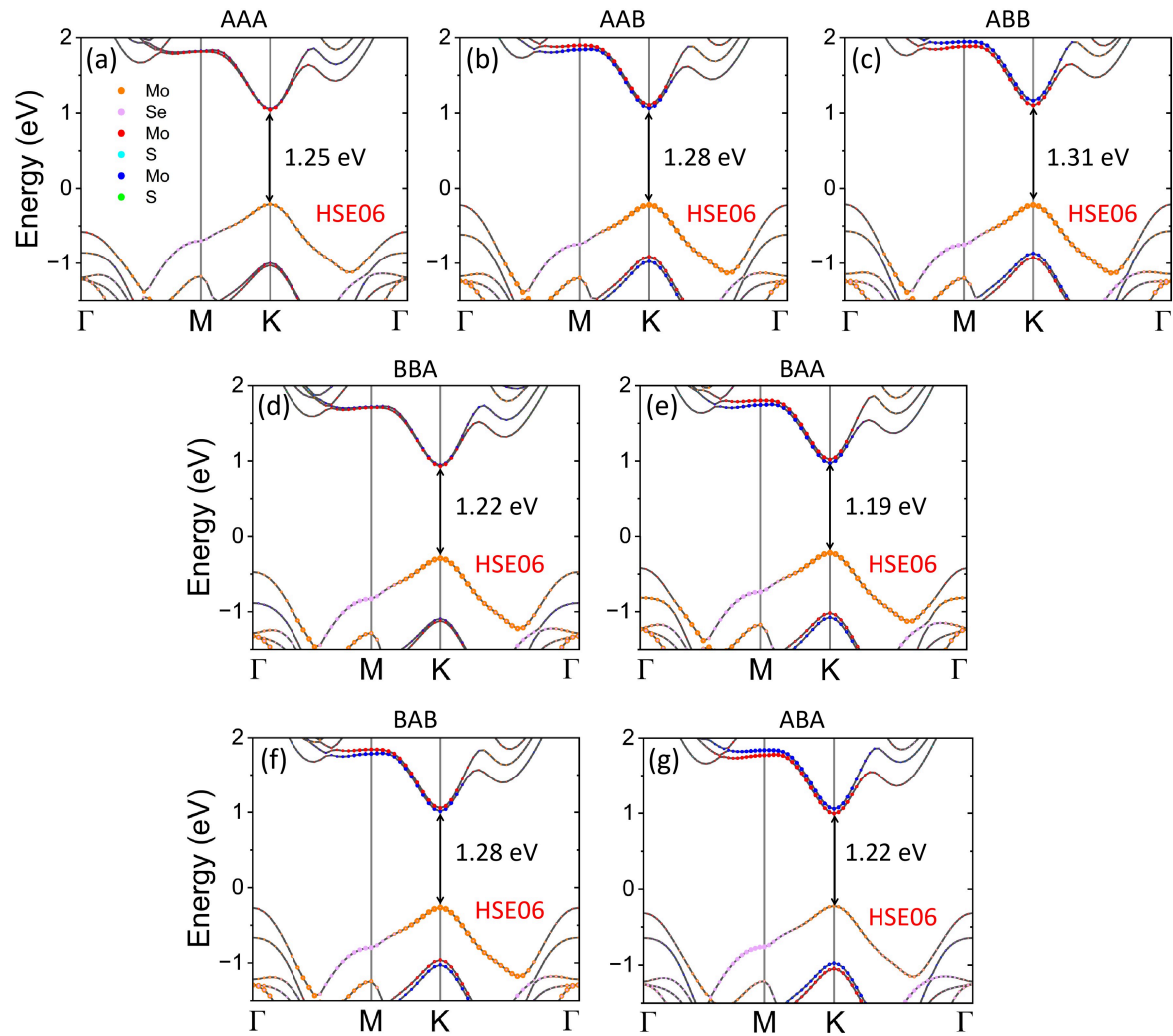


FIG. S13: Electronic band structures calculated using HSE06, showing enhanced band gaps and preserved stacking trends.